

CALCULATION OF THE VAPOR-LIQUID COEXISTENCE
OF POLYMER-GRAFTED NANOPARTICLES

By

Siladitya Mukherjee

Thesis

Submitted to the Faculty of the
Graduate School of Vanderbilt University
in partial fulfillment of the requirements

for the degree of

MASTER OF SCIENCE

in

Chemical Engineering

May 2013

Nashville, Tennessee

Approved:

Peter T. Cummings

G. Kane Jennings

TABLE OF CONTENTS

	Page
ACKNOWLEDGEMENTS.....	iii
LIST OF TABLES.....	iv
LIST OF FIGURES.....	v
CHAPTERS	
1. INTRODUCTION.....	1
2. BACKGROUND.....	4
2.1 Molecular Dynamics (MD) Overview	4
2.2 Applications of Molecular Dynamics.....	11
2.3 Vapor-Liquid Equilibrium (VLE).....	11
2.4 Thermodynamics of Phase Equilibrium.....	13
2.5 Applications of Vapor-Liquid Equilibrium.....	15
3. TETHERED NANOPARTICLE (TNP).....	16
3.1 Tethered nanoparticle anisotropy	17
3.2 Experimental Studies of Tethered Nanoparticles.....	19
3.3 Simulation Studies of Tethered Nanoparticles	24
3.4 Applications of Tethered Nanoparticle	31
4. OBJECTIVE OF THE THESIS.....	32
5. SIMULATION MODEL & METHODOLOGY.....	34
5.1 Coarse-Grained (CG) Model Overview.....	34
5.2 United Atom (UA) Model	37

5.3 Bead Spring Model	38
5.4 Simulation Setup	39
5.4.1 Alkane-Tethered Nanosphere System	39
5.4.2 Alkane-Tethered Amorphous Silica Nanosphere System	41
5.5 Simulation Methodology	46
5.6 Brownian dynamics	46
5.7 Quench Molecular Dynamics	48
6. RESULTS & DISCUSSIONS	50
6.1 Alkane-Tethered Nanosphere System	50
6.1.1 VLE As a Function of Chain Length	50
6.1.2 VLE As a Function of Interaction Strength	52
6.1.3 Comparison With SAFT-VR Equation of State	53
6.2 Alkane-Tethered Amorphous Silica Nanosphere System	56
6.2.1 VLE As a Function of System Size (Tethers are free to move)	57
6.2.2 VLE As a Function of Number of Chains (Tethers are free to move)	58
6.2.3 VLE As a Function of Chain Length (Tethers are free to move)	60
6.2.4 VLE as a function of nanosphere diameter (Tethers are free to move)	63
6.2.5 VLE As a Function of Planar Angle (θ) Between Tethers (Fixed Tethers)	66
6.2.6 Accuracy Test of the Estimated Critical Temperatures (T_c)	69
7. CONCLUSIONS	72
BIBLIOGRAPHY	74

ACKNOWLEDGEMENTS

First of all, I would like to thank Dr. Peter T. Cummings for his advising and allowing me to work in this project. Your input has been invaluable during my graduate research. A special thanks to Dr. C.R. Iacovella for guiding me in every step of this project, without which it would have been difficult to successfully complete this project. Your guidance will always be appreciated. I would like to thank Dr. G. Kane Jennings for his support and guidance during my graduate career. I am very fortunate to have you in my committee. I thank everyone in the Cummings lab who helped make work more enjoyable. A special mention to William French and Junhwan Jeon, I have always learnt a lot from both of them. I would like to thank my friends at Vanderbilt: Gaurav, Tim, Parkishit, Jugantar, Ashish, Anirban, for all their help throughout my stay at Vanderbilt.

I am very grateful to Dr. Clare McCabe and Jessica Haley for providing all the SAFT-VR calculation, which was an instrumental part of this project.

I would also like to thank my undergraduate friends: Deepraj, Souvik, Avisek, Rajdeep, Atanu, Sayanjeet, Subharthi for always being there with me and supporting me.

To my niece Anushka, thank you for always bring a smile to my face. Finally, I would like to thank my parents, my sister and brother-in law for their immense support and love throughout all these years.

LIST OF TABLES

Table	Page
3.1 Applications of polymer tethered nanoparticles.....	31

LIST OF FIGURES

Figure	Page
2.1 (a) Bond-angle interaction. (b) Dihedral interaction with negative φ	8
2.2 Periodic boundary condition in two dimensions with the primary cell surrounded by its image cells.....	10
3.1 Classification of tethered nanoparticle anisotropy.....	18
3.2 Schematic representation of some experimentally synthesized tethered nanoparticles.....	19
3.3 Experimental results of tethered buckyballs.....	20
3.4 The coefficients of thermal expansion (CTE) of the PI-POSS nanocomposites vs amine group ratio.....	21
3.5 Mechanical property (Young's modulus) epoxy/S-clays vs clay Concentration.....	22
3.6 Thermal conductivity of composites containing hybrid filler.....	23
3.7 The conductivity variation curve of PPy/SrFe ₁₂ O ₁₉ nanocomposite.....	23
3.8 Self-assembled tethered-nanoparticle structures.....	25
3.9 Predicted morphologies of model tethered nanorods.....	26
3.10 T^* vs φ phase behavior of polymer tethered nanosphere.....	28
3.11 Images of self-assembled structures of polymer tethered nanosphere with tethers removed for clarity.....	29
3.12 Temperature vs concentration phase diagrams for mono-tethered nanosphere systems.....	30
5.1 Concept of United atoms.....	37
5.2 Bead-spring chain model with spring configurations given by connectors vectors Q_i	38

5.3	(a) Comparison between Lennard-Jones and Girifalco potential (b) formation of a coarse-grained nanosphere.....	40
5.4	Interaction strength comparison between Lee and Hua's model and explicit Si_6O_{12} system.....	42
5.5	Various size spherical nanosphere formation from the bulk system.....	43
5.6	Interaction between 1.2 nm silica nanoparticles.....	44
5.7	Plot of interaction parameters as a function of nanoparticle diameter.....	44
5.8	Workflow for calculating the interaction potential for the amorphous silica nanoparticle system.....	45
5.9	Schematic representation of quench dynamics method.....	49
6.1	Schematic representation of different systems considered for VLE calculation. (a) bare nanoparticle, (b) mono-tethered nanosphere ($n_{\text{totalbeads}}=4$), (c) mono-tethered nanosphere ($n_{\text{totalbeads}}=8$), (d) mono-tethered nanosphere ($n_{\text{totalbeads}}=12$).....	50
6.2	VLE of mono-tethered nanosphere system ($n_{\text{chain}}=1$) at different tether lengths.....	51
6.3	Plot of critical temperature as a function of tether length for alkane-tethered nanosphere system.....	52
6.4	Phase behavior of mono-tethered nanosphere ($n_{\text{totalbeads}}=12$) system at different nanoparticle interaction strength.....	53
6.5	VLE of mono-tethered nanosphere system with simulation (■) and SAFT-VR (●).....	54
6.6	Pressure density isotherms of mono-tethered nanosphere system using SAFT-VR (solid lines) and simulation (symbols).....	55
6.7	VLE of mono-tethered nanosphere system using SAFT-VR theory at different tether lengths.....	56

6.8	Schematic representation of tethered silica nanoparticle system at different anisotropic conditions, (a) mono-tethered, (b) di-tethered, (c) quad tethered, (d) hexa-tethered, (e), (f), and (g) variation of the tether lengths.....	56
6.9	VLE of alkane-tethered silica nanoparticle system as a function of system size.....	57
6.10	VLE of alkane-tethered silica nanoparticle system as a function of number of chains.....	59
6.11	Potential of mean force (PMF) between nanoparticles as a function of number of chains.....	60
6.12	VLE of di-tethered ($n_{\text{chain}}=2$) silica nanoparticle system at different tether lengths.....	62
6.13	VLE of quad-tethered ($n_{\text{chain}}=4$) silica nanoparticle system at different tether lengths.....	62
6.14	VLE of hexa-tethered ($n_{\text{chain}}=6$) silica nanoparticle system at different tether lengths.....	63
6.15	VLE of hexa-tethered ($n_{\text{chain}}=6$) silica nanoparticle system at different nanoparticle diameters.....	64
6.16	VLE of hexa-tethered silica nanoparticle system by conserving the $n_{\text{chains}}/S.A.$ ratio.....	65
6.17	Schematic representation of the model di-tethered silica nanoparticle system with fixed tethers.....	66
6.18	Histogram of the distribution of the planar angle (θ) between tethers at the nanoparticle surface. In this case, the tethers are fixed at 60°	67
6.19	VLE of di-tethered ($n_{\text{chain}}=2$) silica nanoparticle system as a function of planar angle (θ) between tethers at the nanoparticle surface.....	68
6.20	Simulation snapshots of hexa-tethered silica nanoparticle system at different temperatures above the estimated critical temperature.....	70
6.21	Potential energy profile of the hexa-tethered silica nanoparticle system as a function of temperature during the gradual cooling procedure.....	71

CHAPTER 1

INTRODUCTION

The application of nanotechnology in various areas, such as sensors, energy storage, electronics, catalysis etc. demands the ability to manipulate nanoscale objects into functional materials and devices. In recent years advances in synthesis techniques have produced nanoparticles with various geometries, sizes and compositions [1, 2]. The ability to assemble these nanoparticles into specific structures for creating novel functional materials and devices is one of the current challenges in the evolving field of nanotechnology. Top-down approaches, such as casting, have been widely used for manufacturing materials. Other processes, such as X-ray and electron beam lithography [3], have been widely used to alter bulk materials on nanometer scales. But it is an overwhelming task to modify the large number of these building blocks into specific arrangements using the traditional top-down approaches. Instead self-assembly, a bottom-up approach, is generally considered as a promising technique [4-7] to arrange nanoscale building blocks into desired structures by using the interactions between the nano-building blocks (NBBs) as the driving mechanism for the assembly process. There are several key advantages of the bottom-up approach over the top-down approaches: (1) bottom-up assembly allows potentially smaller geometries than photolithography, (2) it is in principle more economical than top-down approaches, in that it does not waste material to etching and does not require the high technology equipment used in

today's multi-billion dollar fabs, (3) large numbers of nano-building blocks can be arranged simultaneously, and (4) highly complex structure formation may be possible with this approach [6, 8].

There exist many natural building blocks that self-assemble into complex structures. For example, viruses can be assembled into a variety of uniquely shape capsides such as icosahedra, tubes, helices, sheets, etc [9]. But there are very few approaches in the literature which offer a comprehensive and generic scheme for nanoparticle assembly. Recent advances in synthesis techniques provide an impressive variety of NBBs of different shapes [1, 2] with many studies demonstrating the functionalization of NBBs with flexible oligomeric, polymeric and biomolecular tethers with specific and non-specific interactions to direct their assembly [6, 10-12]. These functionalized materials, often referred to as tethered NBBs, can be considered as a new class of macromolecule, with the ability to control nanoparticle assembly [11]. Certain classes of tethered NBBs possess characteristics similar to block copolymers (BCPs) and surfactants; as such, ordered microphases often appear that are governed by similar physics, where two or more incompatible species seek to minimize their free energy by aggregating with species of their own kind [12-14]. Other classes of tethered NBBs may behave closer to dipolar or patchy systems [15-17], where strong directional interactions exist, creating strings and other related phases. Understanding how to control and predict the behavior of these systems is of the utmost importance to the creation of next generation functional nanomaterials with specific, desirable properties.

This thesis work presents a novel efficient technique to evaluate the vapor-liquid equilibrium behavior of polymer tethered nanoparticle systems under various anisotropic conditions using molecular dynamics simulations and volume-quench dynamics technique. Additionally, our simulation results are also compared with SAFT-VR, demonstrating good qualitative agreement between simulation and theory. SAFT-VR calculations are used to extrapolate trends to state points difficult to study via simulation alone (e.g., long chains).

This thesis is organized as follows. Chapter 2 provides a brief background of Molecular Dynamics (MD) and its components, applications of MD simulations. Also in this chapter a brief overview of vapor-liquid equilibrium (VLE) and its applications is given. Chapter 3 talks about tethered nanoparticles (TNP), some related experimental and simulation studies of TNPs and the applications of TNPs. Chapter 4 describes the objective of the thesis. Chapter 5 provides detailed simulation model and methodology used for this work. Chapter 6 talks about the results obtained from the simulations and their interpretations. Finally we conclude this thesis with a summary in Chapter 7.

CHAPTER 2

BACKGROUND

2.1 Molecular Dynamics (MD) Overview

Molecular dynamics (MD) is a molecular simulation method based on computing the motions of individual atoms and/or molecules [18-20]. Coupled Newton's equation of motion, which describe the positions and momenta, are solved for a large number of particles in an isolated cluster or effectively in bulk using periodic boundary conditions. The equations of motion for these particles which interact with each other via intra- and inter-molecular potentials can be solved accurately using various numerical integration methods such as the common predictor-corrector or Verlet methods. Molecular dynamics efficiently evaluates configurational and dynamic properties the latter of which cannot generally be obtained by Monte Carlo simulation.

(a) Main principle

The main principle of MD simulation [18] is as follows: given the system state $S(t_0)$, that is, the position r and velocity v of every particle in the system at time t_0 , subsequent states $S(t_0+\Delta t)$, $S(t_0+2 \Delta t)$,....., are calculated by using Newton's law $F = ma$. For accurate results small timesteps Δt have to be used. To calculate $S(t_0+(n+1) \Delta t)$ from $S(t_0+n \Delta t)$, first for every particle i , the force on each particle, $F_i(t_0+n \Delta t)$ is calculated. $F_i(t_0+n \Delta t)$ is the sum of the forces on i as exerted by the other particles of the system at time $t_0+n \Delta t$. For every particle i the force $F_i(t_0+n \Delta t)$ is then

integrated to get the new velocity $v_i(t_0+n \Delta t)$. Using this velocity, for every particle i the new position $r_i(t_0+(n+1) \Delta t)$ can be calculated.

(b) Integration

A widely used, simple and numerically stable, integration algorithm is the Verlet leapfrog algorithm [21]. In this algorithm particle positions are calculated at times $(t_0 + n \Delta t)$ and velocities at midpoints, i.e. at $t_0 + (n + \frac{1}{2}) \Delta t$. With $t_n = t_0 + n \Delta t$.

The equations for leap-frog integration are shown in equation 2.1.1 and 2.1.2.

$$v_i(t_n + \Delta t/2) = v_i(t_n - \frac{\Delta t}{2}) + m^{-1} F_i(t_n) \Delta t \quad (2.1.1)$$

$$r_i(t_n + \Delta t) = r_i(t_n) + v_i(t_n - \frac{\Delta t}{2}) \Delta t \quad (2.1.2)$$

(c) Interaction Forces

Generally, in an MD simulation the forces between particles only depend on particle positions, not on velocities. Usually, interactions are specified by giving an expression for the potential energy of the interaction, hence the force can be written as gradient of the potential.

Two classes of interactions may be distinguished: non-bonded interactions and bonded interactions.

(d) Non-Bonded Interactions

Non-bonded interactions model flexible interactions between particle pairs. Two well known non-bonded interaction potentials are the Coulomb potential and the Lennard-Jones potential [19, 22, 23].

The non-bonded interactions are described by using the following expressions:

- Electrostatic Terms (Coulomb potential)

The electrostatic interactions between two atoms i and j is given by equation 2.1.3.

$$V_{\text{Coul}} = \frac{1}{4\pi\epsilon_0} \frac{q_i q_j}{r_{ij}} \quad (2.1.3)$$

where q_i and q_j are the charges of particle i and j respectively, r_{ij} is the distance between the particles i and j respectively. The Coulomb force on particle i, due to particle j is given by equation 2.1.4.

$$F_{ij \text{ Coul}} = \frac{q_i q_j}{4\pi\epsilon_0} \frac{r_{ij}}{r_{ij}^3} \quad (2.1.4)$$

- Van der Waals Terms (12-6 Lennard-Jones potential)

$$V_{LJ} = 4\epsilon \left[\left(\frac{\sigma}{r_{ij}} \right)^{12} - \left(\frac{\sigma}{r_{ij}} \right)^6 \right] \quad (2.1.5)$$

where ϵ is a constant determining the depth of the potential well, and where σ determines the diameter of the particle. The term $\left(\frac{\sigma}{r_{ij}}\right)^{12}$ models a strong repulsive force at very short distances, and the term $\left(\frac{\sigma}{r_{ij}}\right)^6$ models an attractive force with a longer range interaction. Adding these two terms gives a potential well. The force of the Lennard-Jones interaction exerted on particle i by particle j is given by

$$F_{ij} = 4\epsilon \left[12 \left(\frac{\sigma}{r_{ij}} \right)^{12} - 6 \left(\frac{\sigma}{r_{ij}} \right)^6 \right] \left(\frac{r_{ij}}{r_{ij}^2} \right) \quad (2.1.6)$$

Due to the 'action = -reaction' principle (Newton's third law of motion), the forces between two interacting particles are related by

$$F_{ji} = - F_{ij}$$

So, the force between every particle pair i, j has to be evaluated only once instead of twice. The usual way to evaluate every interaction only once is to use the $j > i$ criterion, i.e., to calculate explicitly the force on the particle with the highest particle number.

(e) Bonded Interactions

Bonded interactions [19] model rather strong chemical bonds, and are not created or broken during a simulation. For this reason, these interactions may be evaluated by running through a fixed list of groups of particle numbers, where each group represents a bonded interaction between two or more particles. The three most widely used bonded interactions are the bond stretch interaction, the bond-angle interaction and the dihedral interaction.

The bond stretch interaction is a bonded interaction between two particles i and j with interaction potential. It is frequently modeled as a harmonic spring viz.

$$V = \frac{1}{2} K_b (r_{ij} - r_0)^2 \quad (2.1.7)$$

The spring has an equilibrium length r_0 and a spring constant K_b .

The bond-angle interaction is a three particle interaction between i, j, k , with interaction potential is frequently modeled as

$$V = \frac{1}{2} K_\theta (\theta - \theta_0)^2 \quad (2.1.8)$$

where, θ is the angle between two bonds to a common atom, θ_0 is the equilibrium length, and K_θ is the force constant.

The dihedral angle interaction $V(\varphi)$ is a four particle interaction between i, j, k, l with an interaction potential $V = V(\varphi)$, and is frequently modeled as

$$V = K \phi (1 + \cos(n \phi - \phi \delta)) \quad (2.1.9)$$

where, φ is the dihedral torsional angle and δ is a constant.

The schematic representation of bond angle interaction and dihedral angle interaction is shown in figure 2.1.

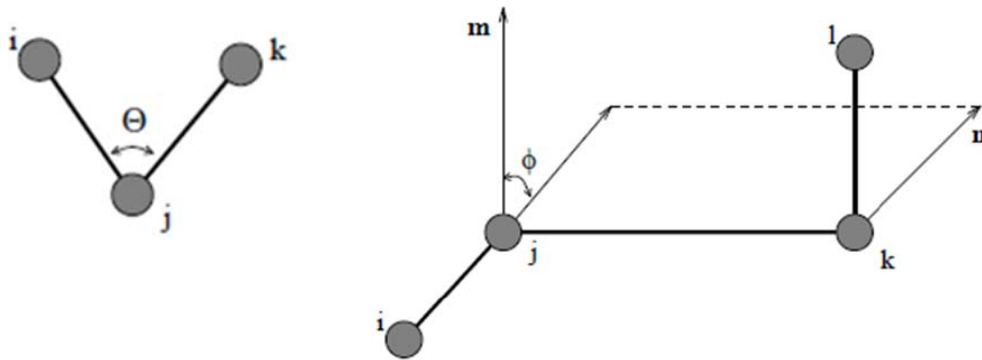


Fig 2.1. (a) Bond-angle interaction. θ is the angle between the lines i, j and k, j , (b) Dihedral interaction with negative φ . m is normal to the i, j, k plane, n is normal to the j, k, l plane.

(f) Cut-Off Radius and Neighbor Searching

In principle, a non-bonded interaction exists between every particle pair. Because most of the CPU time of an MD simulation is spent in non-bonded force calculations, the greatest gain in performance can be achieved by efficiency improvements in this part. Two optimizations are widely applied: the use of a cut-off radius, and the use of neighbor lists [18, 19].

The main contribution to the total force on a particle is from neighboring particles. Therefore, only a small error is introduced when interactions are evaluated between

particles with a distance less than a specified cut-off radius r_{cut} . Choosing r_{cut} so that for each particle 100 to 300 other particles are within cut-off radius gives a good balance between correct physics and efficiency. For a system of 10^4 particles this makes the non-bonded force computation a factor $10^4/100$ to $10^4/300$ faster.

Still when using a cut-off radius, all pairs have to be inspected to see if their separation is less than r_{cut} . This is called neighbor searching. However, the timesteps made are so small that particles travel only a very small distance during one timestep. In other words, the set of particles within r_{cut} of a given particle hardly changes during one timestep. Therefore, only a small error is made when only every 10 or 20 timesteps all pairs are inspected to see if their distance is less than r_{cut} . Pairs with a distance less than r_{cut} are stored in so called neighbor lists which are used the next 10 or 20 timesteps. In this way the all-pairs inspection every timestep is replaced by an all-pairs inspection every 10 or 20 timesteps at the cost of some memory space to store the neighbor list of every particle. Using r_{cut} and a neighbor list, non-bonded force calculations still take about 70% of the total CPU time.

(g) Periodic Boundary Conditions

Molecular dynamics is typically applied to small systems containing thousands of particles. Unless the behaviors near the walls (surface effects) are of interest, they can be eliminated and periodic boundary conditions are employed to simulate the bulk material [19]. Particles are generated in a volume V which is called the primary cell. The bulk is assumed to be composed of the primary cell surrounded by its exact replicas to model a macroscopic sample. The image cells not only have the same size

and shape as the primary one but also contain particles that are images of the particles in the primary cell. Cells are separated by open boundaries so particles can freely enter or leave any cell. When particles leave the cell, their images simultaneously enter the cell through the opposite face. Therefore the shape of the cells must be space filling. The number of image cells needed depends on the range of intermolecular forces. When the forces are sufficiently short ranged (e.g. in truncated Lennard-Jones model), only image cells that adjoin the primary cell are needed (minimum image convention). For squares in two dimensions, there are eight adjacent image cells whereas for cubes in three dimensions, the number of adjacent images is 26. Figure 2.2 illustrates the periodic boundary condition in two dimensions with the primary cell surrounded by eight of its image cells.

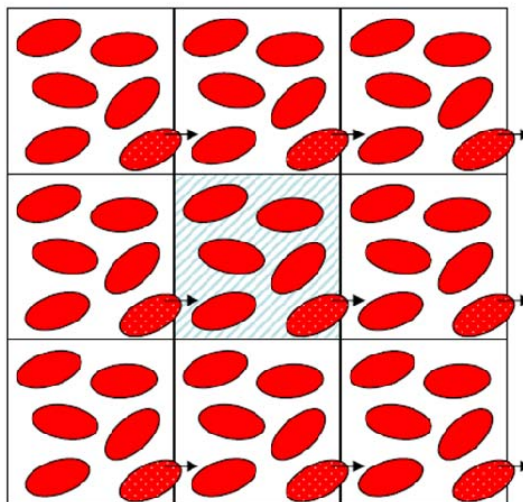


Fig 2.2. Periodic boundary condition in two dimensions with the primary cell surrounded by its image cells. Molecules that leave the cell will be replaced by their images entering the cell from the opposite side.

2.2 Applications of Molecular Dynamics

MD simulations are used to complement and to replace experiments in physics and chemistry. As such, MD has been used to study simple gases, liquids, polymers, crystals, liquid crystals, proteins, proteins in liquids, membranes, DNA-protein interactions [24, 25], etc. For example, the equation of state (the p ; T ; V diagram) or transport phenomena, such as thermal conductivity, diffusivity of a gas, may be calculated by an MD simulation [26]. For polymers MD has been used to calculate mechanical properties like compressibility and tensile strength [27]. In the area of drug design, MD is used to calculate the free energy of binding [28]. Nuclear Magnetic Resonance experiments give incomplete information about inter-atom distances; MD is used to refine these data. Many of the physical properties mentioned are not derived from one system state but as a time average over a long sequence of consecutive states.

2.3 Vapor-Liquid Equilibrium (VLE)

Separation and purification processes account for a large portion of the design, equipment, and operating costs of a chemical plant. Equilibrium between mechanically separable phases is a part of the basis for most of the operations involved in chemical engineering. Most of the separation processes are contact operations and they require a favorable relationship between the equilibrium states of two phases for their success. In distillation [29], a difference in composition between a liquid and a gas phase in equilibrium is essential. The same is true for gas absorption [30]. Liquid extraction [31] requires a difference in composition

between two liquid phases. Other examples are also possible. This design of these processes involves the use of accurate vapor-liquid equilibrium (VLE) data and correlating models or, in the absence of experimental data, of accurate predictive methods. Phase behavior, especially vapor-liquid equilibria [32-36], is important in the design, development, and operation of chemical processes. Because the modeling of vapor-liquid equilibria is a mature subject, one might think that the available activity coefficient models for low-pressure-phase equilibria and various equations of state [37, 38] with the simple van der Waals one-fluid mixing rules for high-pressure applications provide sufficient tools for its treatment. But this perception is not actually correct. For example, activity coefficient models [39-41] for highly non-ideal mixtures are applicable only to the liquid phase but even then, with temperature-dependent parameters. Cubic equations of state [37, 42] with the classical mixing rules can be used over a wide range of temperature and pressure, although only for hydrocarbons and inorganic gases. Also, the use of an activity coefficient model for the liquid phase and an equation of state for the vapor phase are very inaccurate near and above the critical conditions. Therefore, until recently it was very difficult to model non-ideal mixtures of organic chemicals adequately over large ranges of temperature and pressure.

This limitation was a significant problem, for example, in the chemical industry as tons of finished products are produced, and they are obtained from basic or commodity chemicals such as acetone, methanol, water, and so forth [88]. The end products are usually complex molecules for which the conventional modeling methods are not always adequate. The phase behavior of the molecules in the basic

chemicals category is simpler to model; however these chemicals are produced in large quantities with significant global market competition, and thus more accurate modeling of them can have a significant economic impact. Recently it has also been recognized that emissions and waste products of any sort can pose severe environmental problems and must be minimized. Consequently, the design requirements for the manufacture of chemicals are becoming ever more stringent, and any improvements through better modeling that can be made in processes involving even the basic chemicals are important [88].

As a result, throughout the chemical manufacturing spectrum, there is the need for vapor-liquid equilibrium models of good accuracy. This is one of the reasons for the considerable recent activity devoted to the development of more accurate models to describe the vapor-liquid equilibrium of more complex mixtures.

2.4 Thermodynamics of Phase Equilibrium

The starting point for a phase equilibrium calculation is the thermodynamic requirement that the temperature, pressure, and partial molar Gibbs free energy of each species be the same in all phases in which that species is present [88]. That is,

$$\bar{G}_i^I(x_i^I, T, P) = \bar{G}_i^{II}(x_i^{II}, T, P) = \bar{G}_i^{III}(x_i^{III}, T, P) = \dots \quad (2.4.1)$$

where the partial molar Gibbs free energy of species i in phase J , $G_i^J(x_i^J, T, P)$, is

$$\bar{G}_i^J(x_i^J, T, P) = \left[\frac{\partial(N^J \underline{G}^J)}{\partial N_i^J} \right] = \mu_i^J(x_i^J, T, P) \quad (2.4.2)$$

Here T and P are temperature and pressure, respectively, x_i represents all the mole fractions in phase J , \underline{G}^J is the molar Gibbs free energy of the phase. The derivative is

to be taken with respect to the number of moles of species i in phase j with all other mole numbers held constant. The partial molar Gibbs of a species is equal to its chemical potential μ_i .

Eqn. (2.4.1) is an exact relation from thermodynamics. However, in chemical engineering design and process simulation, what are needed are interrelations between the compositions of the phases in equilibrium rather than among the chemical potentials [88]. Consequently, considerable effort in applied thermodynamics is devoted to converting the relation of eqn. (2.4.1), together with the definition of the chemical potential in eqn. (2.4.2), into interrelations between the compositions of the equilibrium phases.

In an ideal homogeneous mixture

$$\overline{G}_i^{\text{IM}}(T, P, x_i) = \underline{G}_i(T, P) + RT \ln x_i \quad (2.4.3)$$

where \underline{G}_i is the pure component molar Gibbs free energy of species i , the superscript IM indicates an ideal mixture, and \overline{G}_i is partial molar Gibbs free energy of species i . Few mixtures are ideal mixtures, and real mixture behavior may be described in terms of departures from eqn. (2.4.3). For liquid mixtures, this is usually done by introducing the activity coefficient, γ_i , of component i in a solution where

$$\overline{G}_i(T, P, x_i) = \overline{G}_i^{\text{IM}} + RT \ln \gamma_i = \underline{G}_i(T, P) + RT \ln x_i + RT \ln \gamma_i \quad (2.4.4)$$

For the ideal solution the activity coefficients of the constituents are unity, and for the real solutions they are defined with respect to a suitable reference state with the limitation that the temperature of the reference state must be that of the solution.

With equations of state, real mixture behavior is described by introducing the

fugacity, f .

The fugacity of a species in a real mixture is

$$\bar{f}_i(T, P, x_i) = x_i f_i(T, P) \exp \left[\frac{\bar{G}_i(T, P, x_i) - \bar{G}_i^{\text{IM}}(T, P, x_i)}{RT} \right] \quad (2.4.5)$$

where $f_i(T, P)$ is the pure component fugacity of the species at the temperature and pressure of the mixture. A fugacity coefficient is defined as

$$\bar{\phi}_i(T, P, x_i) = \frac{\bar{f}_i(T, P, x_i)}{x_i P} \quad (2.4.6)$$

Using the fugacity, the equilibrium relation of eqn. (2.4.1) becomes

$$\bar{f}_i^{\text{I}}(x_i^{\text{I}}, T, P) = \bar{f}_i^{\text{II}}(x_i^{\text{II}}, T, P) = \bar{f}_i^{\text{III}}(x_i^{\text{III}}, T, P) = \dots \quad (2.4.7)$$

2.5 Applications of Vapor-Liquid Equilibrium

Processes taking advantage of favorable vapor-liquid distributions of components form by far the most extensive list of processes in which phase equilibrium is important. Distillation [29], the most important process of the chemical and petroleum industries, is the classical example of an operation whose success is determined by a favorable distribution between vapor and liquid phases. There are, however, other operations of importance involving vapor-liquid equilibrium. Gas absorption [30, 43], azeotropic distillation [44], extractive distillation, humidification and dehumidification, evaporation and flashing of liquid mixtures are all operations based on vapor-liquid equilibrium. Because there are so many applications of vapor-liquid equilibrium, techniques for calculation and experimental determination of this particular type of phase equilibrium are extremely important and are more highly developed than for any other.

CHAPTER 3

TETHERED NANOPARTICLE (TNP)

It is well known that the aggregation/dispersion of nanoparticles can have a significant impact on the properties of the system. One approach to control the aggregation is to create tethered nanoparticle building blocks, where polymers are grafted to the nanoparticles. The resulting behavior of the tethered system is dictated by the contributions from both the nanoparticles and polymers, and it is possible to alter the structure and properties of these systems by tuning these interactions [45-47]. In some cases, these tethered nanoparticles behave like BCP or surfactants, where their assembly is driven by the immiscibility between nanoparticles and tethers. Such systems are also commonly referred to as “shape amphiphiles” [11]. For example, if tethers and nanoparticles dislike each other, these building blocks can phase-separate into various structures such as lamellae, cylinders, gyroids, etc. More complex structures can be obtained by changing the shape of the nanoparticle, such as adding additional liquid crystalline ordering for rod-like nanoparticles [48-52]. It is also possible to alter the properties of a nano-building block system by tuning the interactions between the nanoparticle and polymer, as well as adjusting the conformational freedom of the polymer grafts [53]. The basic design concept behind tethered nanoparticles is to create building blocks with anisotropic interactions [6], and this functionalization of the nanoparticles with tethers in an anisotropic manner causes the building blocks to act as their own

“templates” for self assembly where the size, shape and architecture of the tethering dictate the structure and properties of the system. The resulting assemblies have broad utility in the area of nanotechnology, physical sciences and biology [10, 54].

3.1 Tethered nanoparticle anisotropy

It is also important to explore the various possible anisotropies associated with the tethered nanoparticles to understand the formation of the vast array of possible self-assembled structures [22]. For example, tethered nanorods may adapt local packings different from tethered nanospheres as a result of asphericity associated with the rod. While less obvious than shape, some other possible ways to manipulate the anisotropy of tethered nanoparticles is to adjust (1) the number of tethers, (2) the length of tethers, (3) the relative placement of tethers on the nanoparticle surface, and (4) tether interaction specificity. Each of these anisotropies can have significant impact on the self-assembled structures. For example, attaching tethers to the nanoparticle may shield the strong nanoparticle-nanoparticle interactions and as more tethers are attached, more shielding of interactions will occur. As such, the structures formed by the mono-tethered nanosphere can be significantly different than the di-, quad-, or hexa- tethered nanosphere [10, 12, 22, 55]. The length of the tethers can also change the balance of the interactions that drive the assembly. The relative location of tethers may impart strong directionality of tether-tether interactions, or even result in patchy colloids [56], which could exhibit behavior similar to a permanent dipole moment. Previous simulations of dipolar hard sphere [57] and also of Stockmayer fluids [58] have revealed that the

anisotropy of the dipolar potential promotes the formation of self-assembled aggregates like chains, rings and more complex clusters. As such, to develop a theoretical framework for the rational design of functional materials and devices for various applications, it is extremely important to understand how each of these anisotropies influences tethered nanoparticle assembly and properties [55, 56, 59]. In figure 3.1 key axes of anisotropy for tethered nanoparticles are shown. In fig axes A classifies number of tethers attached to the nanoparticle.

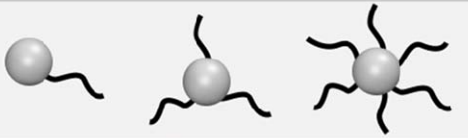


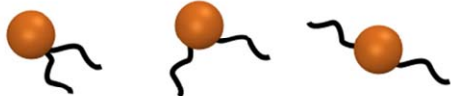
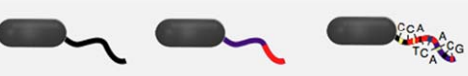
Number of tethers	A	
Relative tether length	B	
Particle shape	C	
Tether placement	D	
Specific/non-specific interactions	E	

Fig 3.1. Classification of tethered nanoparticle anisotropy. (A) Number of tethers, (B) Relative length of tethers/relative size of nanoparticle, (C) Number of nanoparticle vertices, (D) Relative location of tethers, (E) Tether interaction specificity (adapted from [22]).

Axis B classifies the relative length of the tether. Axis C refers to the nanoparticle shape. Axis D classifies the placement of the tethers on the nanoparticle. Axis E classifies the specificity of the tether-tether interactions.

3.2 Experimental Studies of Tethered Nanoparticles

Many examples of experimentally synthesized tethered nanoparticles have recently been reported in literature. Figure 3.2 shows the schematic representation of some experimentally synthesized building blocks.

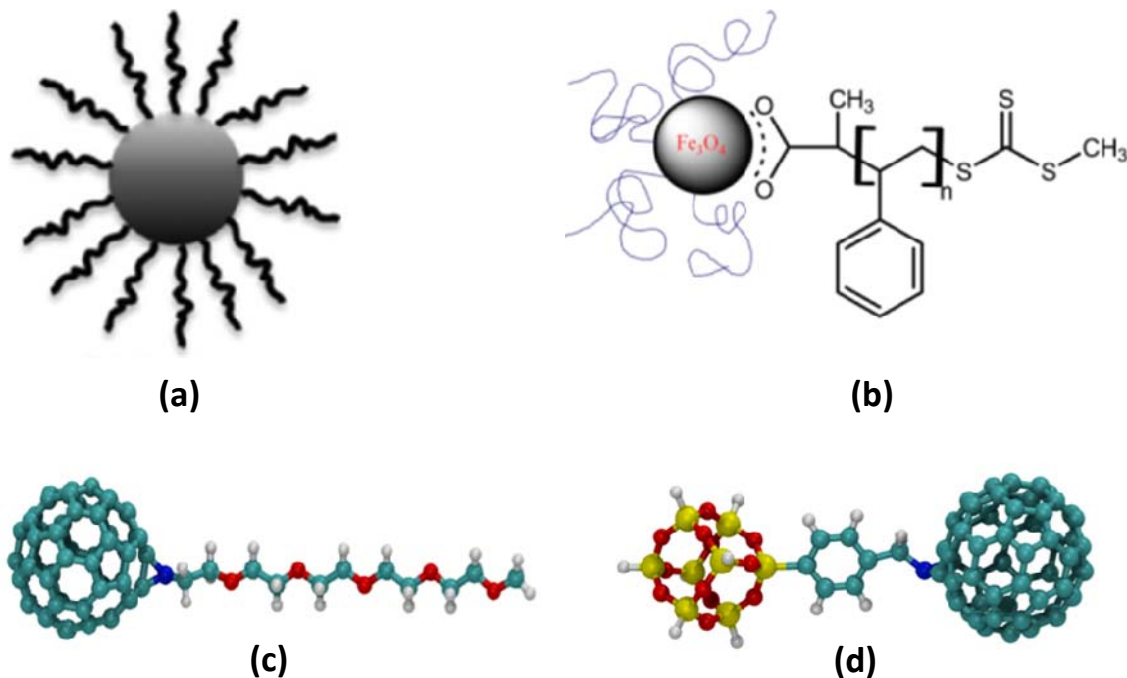


Fig 3.2. Schematic representation of some experimentally synthesized tethered nanoparticles. (a) Poly ethylene glycol (PEG) tethered SiO_2 nanoparticle [60], (b) Polystyrene (PS) grafted Fe_3O_4 nanoparticle [61], (c) tethered buckyball [8] , (d) telechelic POSS buckyball [62].

Song et al. [8] synthesized buckyballs with poly ethylene oxide (PEO) tethers attached (schematic shown in fig 3.2 (c)). In this work they investigated the effect of miscibility and C_{60} concentration on the aggregation behavior of the PEO tethered buckyball. They found the formation of spherical and wormy micellar aggregates as a result of the strong hydrophobicity of buckyball. They also found that changing the solvent from tetrahydrofuran to water could be used to change the aggregation

behavior of the telechelics from spherical to wormy micellar aggregates. The Transmission electron microscopy (TEM) micrographs of tethered buckyballs in tetrahydrofuran (THF) and water are shown in figure 3.3.

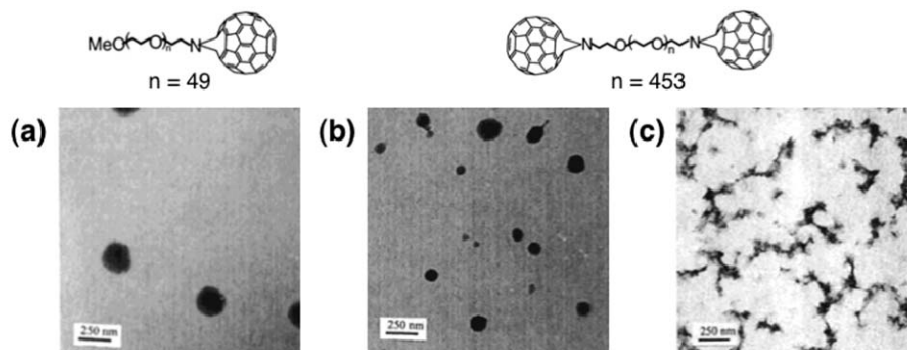


Fig 3.3. Experimental results of tethered buckyballs (a) Spherical micelles formed by mono-tethered buckyballs in tetrahydrofuran, (b) spherical micelles formed by telechelic buckyballs in tetrahydrofuran and (c) wormy micelles formed by telechelic buckyballs in water (adapted from [8]).

The TEM images in figure 3.3 (a) and 3.3 (b) show the formation of spherical micelles by the mono-tethered and telechelic buckyballs in THF. Fig 3.3 (c) shows the wormy micellar aggregate formation by telechelic buckyballs in water. The mechanical properties of telechelic buckyball were demonstrated to be substantially enhanced as compared to the polymer tethers alone. For example, fracture toughness of the telechelic system was increased by 2700 times compare to the polymer alone and the telechelics could also sustain large plastic deformations of > 640% before fracture; in both cases, the enhanced behavior was associated with the network-like structures that form for tethered buckyballs [63]. Westenhoff and Kotov developed CdTe quantum dots tethered to a polyelectrolyte film via anionic poly ethylene glycol (PEG) tethers [64]. They demonstrated that this PEG-tethered CdTe quantum dots is an example of organized nanoparticle system with tunable

optical coupling. Akcora and coworkers created polymer-grafted silica particles, finding that aggregate structure can be controlled via the grafting density and length of the grafts [10]. Huang et al. made Polyimide (PI)/POSS nanocomposites and they observed the improvement in the thermal stability and mechanical property such as high glass transition temperature (T_g) and low coefficient of thermal expansion (CTE) of the nanocomposites resulted from the strong covalent bonds between PI and POSS molecules [65]. Figure 3.4 shows plot of the coefficient of thermal expansion (CTE) vs the amine group ratio.

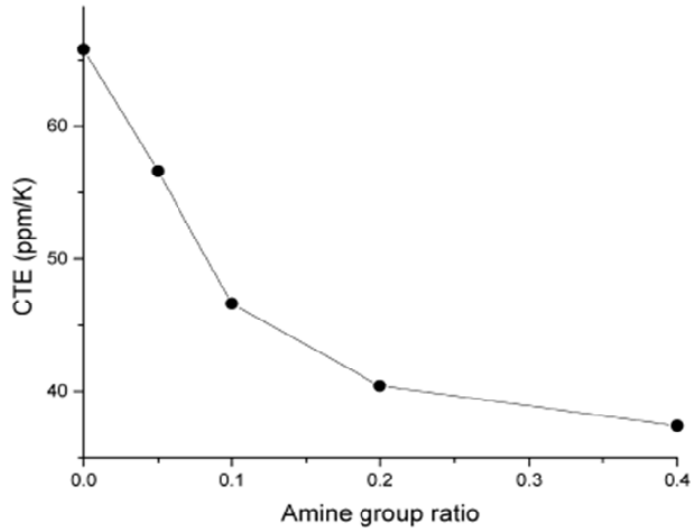


Fig 3.4. The coefficients of thermal expansion (CTE) of the PI-POSS nanocomposites vs amine group ratio (adapted from [65]).

The CTEs of the PI-POSS nanocomposites decrease dramatically with the increase in the amine group ratio as can be seen from fig. The CTEs of the pure PI and the PI-POSS nanocomposites of 0.1 amine group ratio are 65.8 and 46.6 ppm/K, respectively. When the amine group ratio increases to 0.4, the CTE of the PI-POSS nanocomposite decreases to 37.4 ppm/K, which is less than 60% of the CTE of pure

PI. Lu et al. prepared ZnS/ polyimide (PI) nanocomposite and found the improvement in mechanical properties and the glass transition temperature of nanocomposites [66]. Wang et al. synthesized epoxy/clay nanocomposites using a “slurry-compounding” process [67]. They found the improvement in Young’s modulus and fracture toughness of the nanocomposite with the incorporation of clay shown in figure 3.5.

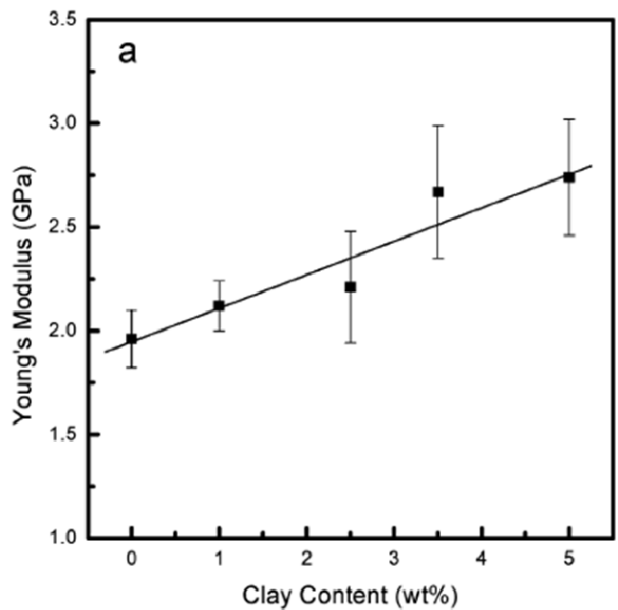


Fig 3.5. Mechanical property (Young’s modulus) epoxy/S-clays vs clay concentration (adapted from [67]).

Lee et al. reported that HDPE/filler nanocomposites were prepared using a mixer and fillers were used such as Wollastonite, SiC, and BN [68]. The thermal conductivity of HDPE nanocomposites was increased with increasing filler content which is shown in figure 3.6.

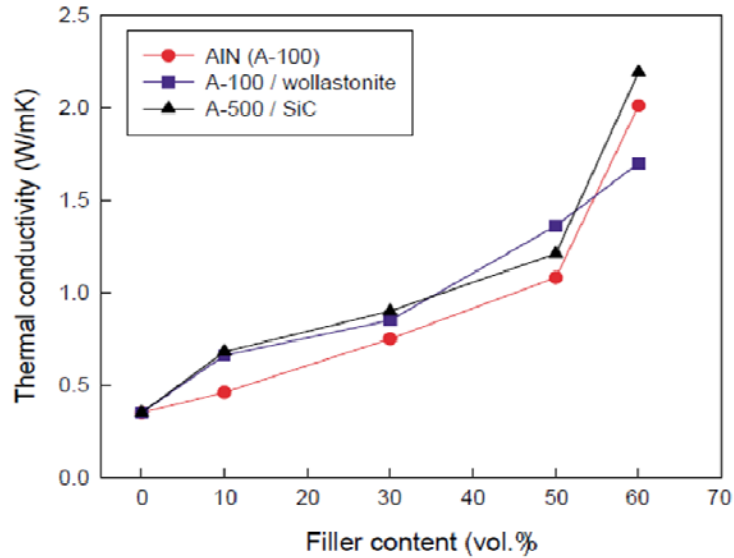


Fig 3.6. Thermal conductivity of composites containing hybrid filler (adapted from [68]).

Zhang et al. synthesized polypyrrole (PPy)/nano-SrFe₁₂O₁₉ nanocomposites by in situ polymerization [69]. They observed the increase in conductivity for the polymer nanocomposites compared to that of the pure PPy. Figure 3.7 shows the conductivity variation curve of PPy/SrFe₁₂O₁₉ nanocomposite.

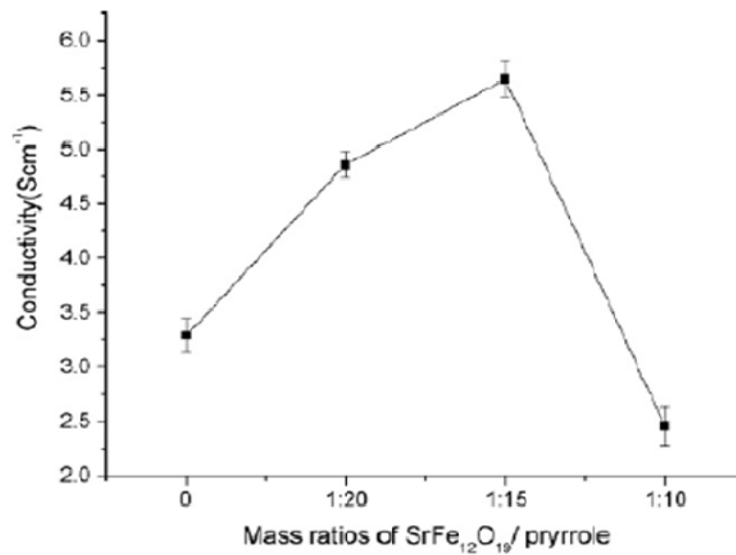


Fig 3.7. The conductivity variation curve of PPy/SrFe₁₂O₁₉ nanocomposite (adapted from [69]).

It can be seen from figure 3.7 when the mass ratio of $\text{SrFe}_{12}\text{O}_{19}$ to pyrrole was less than 1:15, the conductivity (5.65 S/cm) of the PPy/ $\text{SrFe}_{12}\text{O}_{19}$ nanocomposite was found to be higher than that of the pure PPy (3.29 S/cm) despite the insertion of the insulating $\text{SrFe}_{12}\text{O}_{19}$ particles.

The above examples signify that by varying nanoparticle and tether geometry and chemistry tunable properties of the composite system can be achieved.

3.3 Simulation Studies of Tethered Nanoparticles

Molecular simulation is a very useful technique for the study of tethered nanoparticles and it can provide insight into the conditions under which various structures may be formed. It is also very trivial in simulation to vary many of the key building block parameters in order establish trends and readily test hypotheses that otherwise might be very difficult to achieve in experiment. Simulation methods have been widely used to gain insight of the structures and properties of the tethered nanoparticles.

Zhang et al. [22] first proposed a simulation framework for modeling and predicting the self-assembly of tethered nanoparticles into bulk ordered structures. Simulations were performed using coarse-grained models of tethered nanoparticles. Briefly, those models used bead-spring representations of the polymers and rigid-body dynamics of collections of point particles to model the geometry of non-spherical nanoparticles. In their work, they demonstrated that the thermodynamic immiscibility of tethers and rigid nanoparticles, arising from condition where the solvent is preferential for either one of those components, can lead to highly

ordered nanostructures which closely resemble the self-assembled phases observed in conventional BCPs, surfactants and liquid crystalline systems. This study highlighted several key parameters that could be used to control the global and local structure of tethered nanoparticle assemblies. Figure 3.8 shows the different self-assembled structures formation by tethered nanoparticles at various anisotropies and at different solvent conditions.

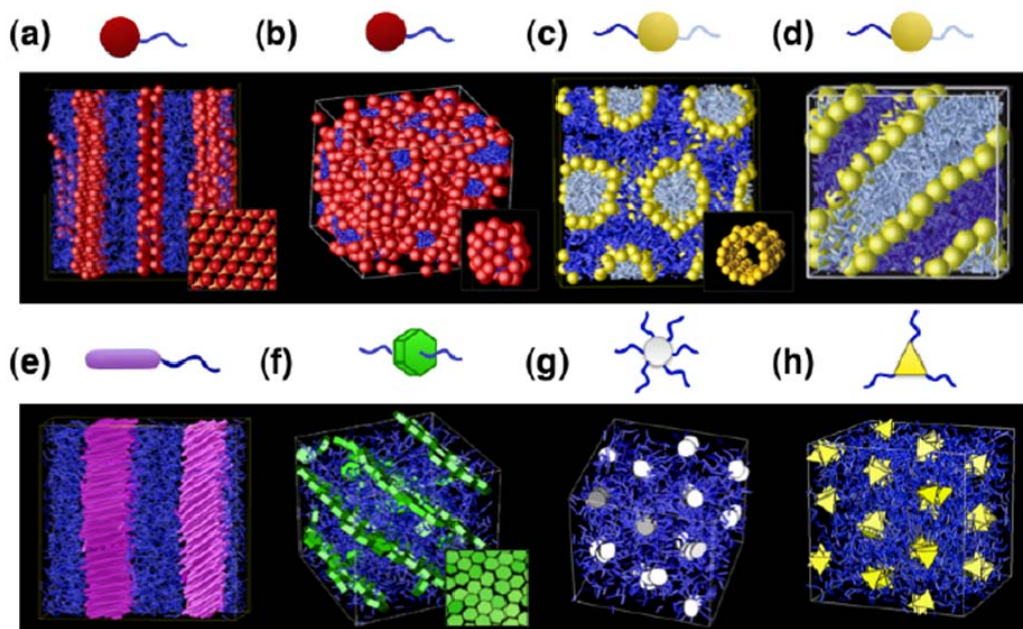


Fig 3.8. Self-assembled tethered-nanoparticle structures (a) Crystalline bilayers formed from mono-tethered nanospheres where the solvent is poor for the nanosphere, (b) Spherical micelles formed by mono-tethered nanospheres where the solvent is poor for the tether, (c) Hexagonally packed cylindrical shells formed by di-tethered nanospheres where solvent is poor for the cyan tether and nanosphere, (d) Lamellar monolayer structure formed from di-tethered nanospheres at a higher volume fraction than in (c), (e) Smectic C lamellar structure formed by tethered nanorods where solvent is poor for the nanorods, (f) Lamellar Monolayers formed by face-tethered hexagonal nanoplates where nanoplates are in poor solvent, (g) Hexagonally packed cylinders formed by equatorially tethered nanoplates where nanoplates are in poor solvent. (h) Hexagonally ordered cylinders formed by triangular tethered nanoplates where nanoplates are in poor solvent (adapted from [22]).

Molecular simulations are also used to predict the phases formed by self-assembly of nanorods functionalized by a polymer tether [51]. A coarse-grained, particle-based model with Brownian dynamics (BD) was used to study the phase behavior of a solution of tethered rods in three dimensions. Microphase separation of the immiscible tethers and rods coupled with the liquid crystal ordering of the rods induced the formation of different self-assembled phases. The detailed morphologies of tethered nanorods obtained from this study are shown in figure 3.9.

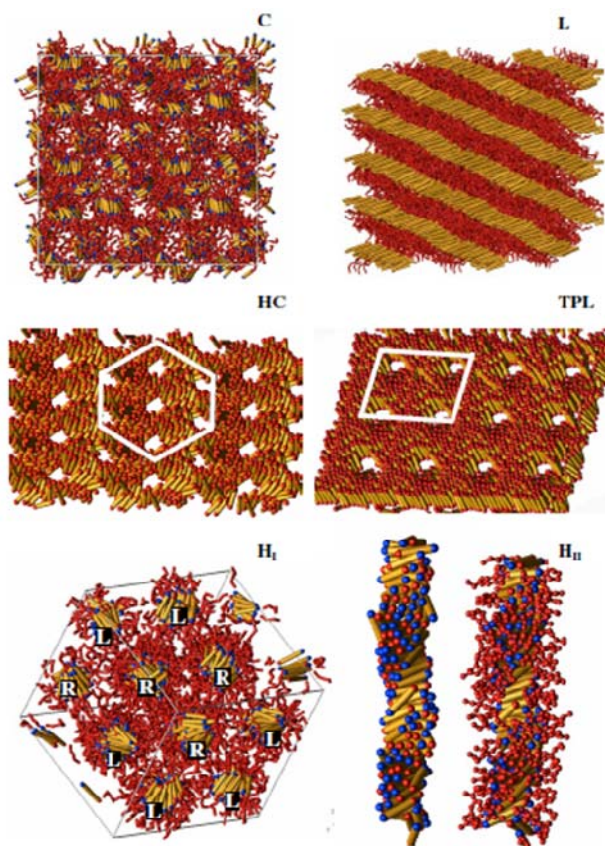


Fig 3.9. Predicted morphologies of model tethered nanorods. (C) Cubic micelle phase. (L) Smectic C phase. (HC) Single sheet extracted from the honeycomb phase “HC.” (TPL) Single sheet extracted from the tetragonally perforated lamellar phase “TPL.” (H_I) Hexagonal chiral cylinder phase. (H_{II}) Individual chiral cylinder from hexagonal cylinder phase without tethers (left) with tethers (right) (adapted from [51]).

A Cubic micelle phase (C) for volume fractions between $\phi = 0.1$ and 0.17 has been observed. The formation of a 3D tetragonally perforated lamellar (TPL) phase and honeycomb (HC) phase was predicted for $\phi = 0.31-0.36$. At higher volume fraction $\phi = 0.36-0.44$, a layered smectic C (lamellar) phase was also found. The TPL and HC phases have been observed in experiments also.

The formations of bulk-phase microstructures formed by single polymer-tethered nanospheres were also examined with attractive particles and repulsive tethers using molecular dynamics simulation in ref. [70]. Here a generic model of tethered nanoparticles were considered, where nanospheres were modeled as beads of diameter 2.0σ connected to tethers via finitely extensible nonlinear elastic (FENE) springs. Tethers were modeled as bead-spring chains containing eight beads of diameter σ connected via FENE springs. The Lennard-Jones potential was used to model the attractive interaction between nanoparticles and Weeks-Chandler-Anderson (WCA) soft-sphere potential was used for the interaction of solvophilic tethers and species of different types. The plot of T^* vs volume fraction (ϕ) phase behavior of the tethered nanoparticle system from this study is shown in figure 3.10.

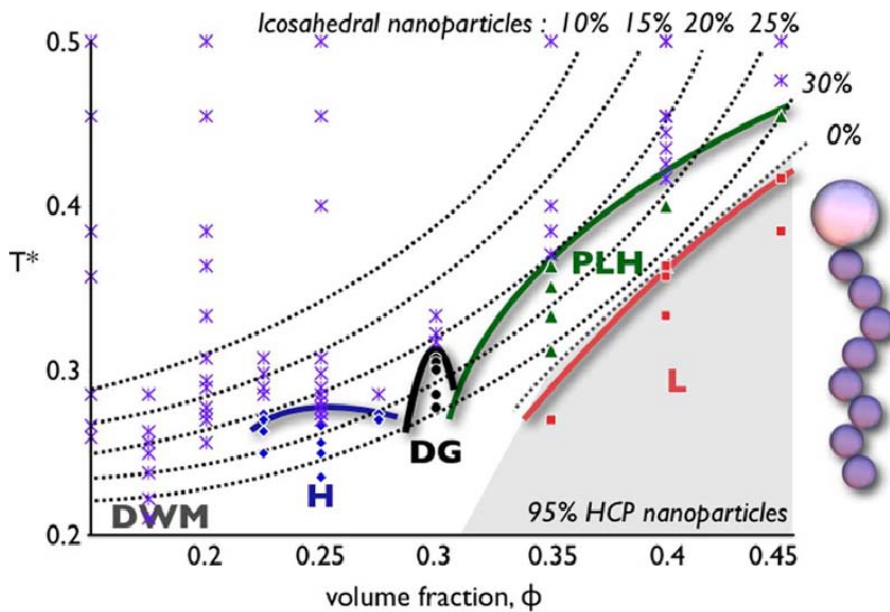


Fig 3.10. T^* vs ϕ phase behavior of polymer tethered nanosphere, where solid lines represent approximate phase boundaries determined by ~ 250 state points. Stars indicate simulated disordered phases. The shaded region indicates the range of T^* and ϕ over which crystalline ordering of the NPs is observed. A schematic of the model tethered nanosphere is shown at right (adapted from [70]).

As can be seen from figure 3.10. at higher ϕ , two phases were observed, lamellar bilayers (L), where hexagonal ordering of nanospheres were found within the lamellar sheets, and the perforated lamellar structure (PLH) where nanospheres demonstrated icosahedral local ordering. The lamellar bilayer phase occurred at lower temperature than the perforated phase. The formation of a double gyroid (DG) phase, where also nanospheres demonstrated icosahedral local ordering, was also found at lower ϕ than perforated lamella. The formation of icosahedra resulted in the reduction of packing frustration within the nodes of double gyroid structure. For low values of ϕ , hexagonally ordered cylindrical micelles (H) were found. For these systems, a stable spherical micelle phase was not observed, instead,

disordered wormy micellar aggregates (DWM) were observed at low ϕ . The images of the self-assembled phases are shown in figure 3.11.

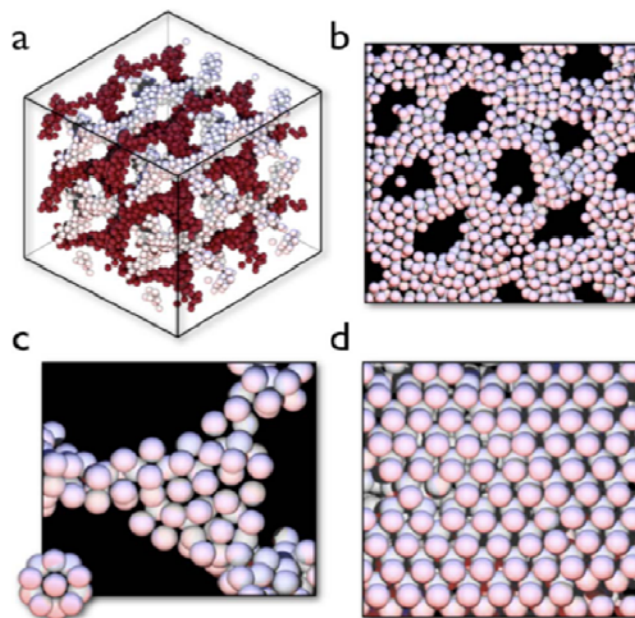


Fig 3.11. Images of self-assembled structures of polymer tethered nanosphere with tethers removed for clarity. (a) DG phase; the minimal unit cell was duplicated and found to be stable over ~ 10 million time steps, (b) Individual sheet of PLH, (c) Node of the DG, showing icosahedral rings; perfect icosahedron inset, (d) Crystalline packing of L (adapted from [70]).

The self-assembled structures formation by the mono-tethered nanosphere shape amphiphiles are explored in ref. [12] and compared with the structures and phase behavior of standard surfactants. The investigations were performed for a wide range of concentration and nanoparticle diameters to understand the range of self-assembled structures, demonstrating under what conditions tethered nanoparticles phase behavior can be approximated by previously established surfactant models. The temperature vs concentration phase diagram of the tethered nanosphere system is shown in figure 3.12.

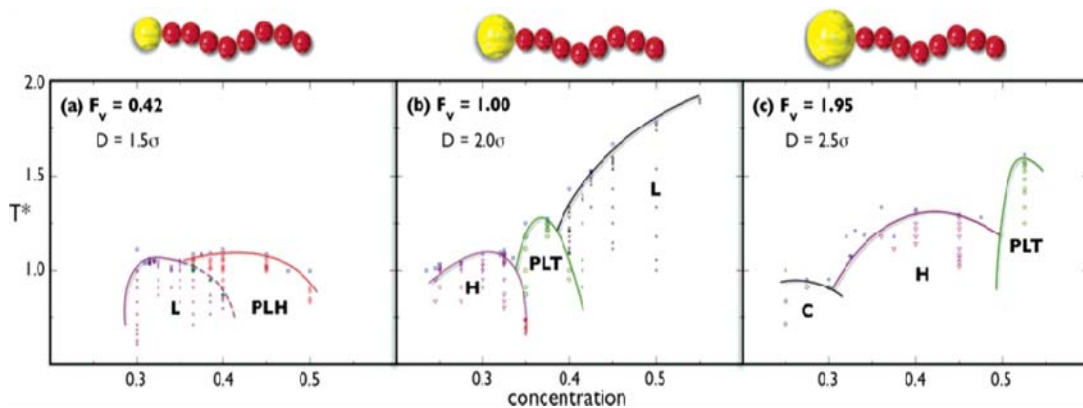


Fig 3.12. Temperature vs concentration phase diagrams for mono-tethered nanosphere systems. Data points indicate performed runs. Phases are defined as lamellae (L), perforated lamellae through the headgroup (PLH), hexagonally packed cylinders (H), perforated lamellae through tethers (PLT), cubic ordered spherical micelles (C). (a) Phase diagram for TNS with particle diameter $d = 1.5\sigma$, (b) particle diameter $d = 2.0\sigma$, (c) particle diameter $d = 2.5\sigma$ (adapted from [12]).

The formation of cubic micelles, hexagonal cylinders, lamellar bilayers, perforated lamellar sheets were observed for certain nanoparticle diameters, concentration and temperature. Those phases strongly resemble the phases observed in surfactant systems. It was also observed from this study that for small nanoparticles relative to tether size the equilibrium structures favor sheet like morphologies and for nanoparticles that are as large as or larger than the tethers, curved morphologies are favored.

There are many other experimental and simulation studies related to the synthesis, assembly and properties of tethered nanoparticles [17, 60, 61, 71-73]. The above examples demonstrate the significance of functionalization of nanoparticles with polymer tether to control the assembly of nanoparticles towards the goal of self-assembling target structures with desired properties. Many experimental, simulation and theoretical studies demonstrated that the alteration of structures

and properties of these systems can be done by controlling various parameters such as nanoparticle shape, size, tether location, tether architecture, solvent selectivity etc. The future of self-assembled polymer nanocomposites will rely on the ability to both predict the optimal building blocks for specific functional materials, but also in the ability to purposefully create such building blocks experimentally.

3.4 Applications of Tethered Nanoparticle

Tethered nanoparticles can be widely used for various industrial applications. The applications of some nanocomposite materials are shown below in table 3.1.

Nanocomposites	Applications
Polycaprolactone/SiO ₂	Bone-bioerodible for skeletal tissue repair
Polyimide/SiO ₂	Microelectronics
PMMA/SiO ₂	Dental applications, optical devices
PLA/LS	Lithium battery development
Nylon-6/LS	Automotive timing-belt
Nylon-6/clay	Barrier films
Polypropylene/clay	Packaging
PET/clay	Food packaging applications
Epoxy/MMT	Materials for electronics
SPEEK/laponite	Direct methanol fuel cells

Table 3.1. Applications of polymer tethered nanoparticles

CHAPTER 4

OBJECTIVE OF THE THESIS

The experimental and simulation studies of tethered nanoparticles (TNP) shown in the previous section signify the potential of TNPs to alter the structure and properties of the composite system. In this regard; properties such as the vapor-liquid equilibrium (VLE) behavior of TNPs is of interest for the future utilization of nanoparticles in functional devices and processing applications. Understanding and tuning the coexistence envelope of TNPs may be of particular significance for improved separations. Many previous studies can be found in the literature which demonstrates the use of molecular dynamics (MD) simulation to study the VLE behavior of different systems at variety of conditions. For example, Holocomb et al. investigated the VLE behavior of Lennard-Jones (LJ) fluid by using MD simulation [34]. The formation of very smooth density profiles were found from this study compared to the previous works. Gelb and Muller introduced temperature-quench MD simulation to investigate the VLE behavior of LJ fluid [23]. In this method simulations were performed using NVT ensemble and the temperature of the system was abruptly lowered during the simulation to create a mechanically and thermodynamically unstable condition, which resulted in the formation of liquid and vapor phases. Density histograms for two phases were calculated by ignoring the effect of interfaces. The authors found excellent agreement of the VLE results of pure LJ fluid compared to the equation of state of Johnson et al. In a more recent

study, In't Veld et al. performed MD simulations to investigate the VLE behavior for pure nanoparticles of various sizes [36]. In their work, three different nanoparticle interactions models were used to calculate the coexistence behavior. The authors found that the coexistence behavior is strongly dependent on the form of the interaction potential between nanoparticles. Significant changes in the trend in critical temperatures were observed from one model to another model. All the above examples provide calculations of VLE behavior of either the pure LJ fluid or the pure nanoparticle system, but till date no comprehensive simulation studies of the VLE behavior of TNP systems has been published. In this work, we have performed a novel calculation of the VLE behavior of n-alkane tethered generic nanosphere system and alkane tethered amorphous silica nanoparticle system using molecular dynamics simulations and volume-quench dynamics technique. The initial purpose is to understand how tuning the interactions between nanoparticle and tether can impact the properties of TNPs. In this study, we treat polymer tethers as n-alkanes, as they are conceptually simple with well-defined interactions, and well established phase coexistence. The coexistence behavior is investigated as a function of the length of the alkane tether, nanoparticle interaction strength, total number of tethers attached to the nanoparticle, nanoparticle diameter and planar angle (θ) between tethers at the surface of the nanoparticles. Additionally, our simulation results are also compared with SAFT-VR equation of state to understand the qualitative agreement between simulation and theory.

CHAPTER 5

SIMULATION MODEL & METHODOLOGY

In order to predict the behavior of tethered nanoparticles (TNP) accurately, it is important to utilize a model that can accurately and efficiently capture the important physics and chemistry at hand. In this work, we focus on a coarse-grained (CG) model of TNP, generic enough to be applicable to a wide range of systems, but with parameters easily relatable to realistic systems. The advantage of using CG model is that it greatly reduces the overall number of forces that must be computed for each time step.

5.1 Coarse-Grained (CG) Model Overview

The first computer simulation of liquids was carried out by Metropolis et al. [38]. The model was an idealized two-dimensional representation of molecules as rigid disks. Only few years later, the simulation was carried out on the three dimensional Lennard-Jones fluids [74] which made it possible to compare data obtained from experiments with computer-generated data. In the late 1950s, the molecular dynamics method was first introduced to study the interactions of hard spheres [75]. Nowadays simulation of materials can be performed at different scales, from a coarse grained approach to a fully atomistic model. Although the fully atomistic method is more accurate, it is computationally expensive due to a large

number of degrees of freedom and provides a large amount of data that is sometimes irrelevant to the properties studied. For macromolecular systems, the coarse-grained approach is widely used as the modeling process is simplified, hence becomes more efficient, and the characteristic topological features of the molecule can still be maintained. The level of detail for a coarse-grained model varies for different cases. The whole molecule can be represented by a single particle in a simulation and interactions between particles incorporate average properties of the whole molecule. With this approach, the number of degrees of freedom is greatly reduced. Different polymers have been modeled using this method [76, 77]. On the other hand, a segment of a polymer molecule can also be represented by a particle (bead). Using this method, branched polymers of different architectures have been successfully simulated [78]. The first coarse-grained model was called the 'dumbbell' model. In this model molecules are treated as a pair of beads interacting via a harmonic potential. However by using this model, it is possible to perform kinetic theory derivations and calculations for nonlinear rheological properties and solve some flow problems. The analytical results for the dumbbell models can also be used to check computer simulation procedures in molecular dynamics and Brownian dynamics [79]. After that, the bead-rod and bead-spring model were introduced to model chainlike macromolecules. Beads in the bead-rod model do not represent the atoms of the polymer chain backbone, but some portion of the chain. These beads are connected by rigid and massless rods. In the bead-spring model, a portion of the chain containing several hundreds of backbone atoms are replaced by a "spring" and the masses of the atoms are concentrated in the mass of beads.

If the springs are taken to be Hookean springs, the bead-spring chain is referred to as a Rouse chain or a Rouse-Zimm chain. This approach has been applied widely as it has a large number of internal degrees of freedom and exhibits orientability and stretchability. However the disadvantage of this model is that it does not have a constant contour length and can be stretched out to any length. Therefore in many cases finitely extensible springs with two parameters, the spring constant and the maximum extensibility of an individual spring, can be included so the contour length of the chain model cannot exceed a certain limit.

In this study, we used a CG model of TNPs in which atoms within an individual nanoparticle are represented by a single coarse-grained particle. CG models have been proposed for several nanoparticles, most notably the Girifalco potential for buckyballs [80]; in this case, the number of force calculations required per timestep is reduced by a factor of 60^2 in absence of cutoff, with minimal impact on many of the observable properties. For polymer systems, calculations can also be simplified by using a united atom approach, where, for example, hydrogen atoms attached to a given carbon are lumped into a single bead. Martin and Siepmann developed a united atom model within the TRAPPe framework [81] for *n*-alkanes which can successfully reproduce the vapor-liquid coexistence behavior of these systems at significantly reduced cost over fully atomistic models.

5.2 United Atom (UA) Model

Normally all atoms are treated explicitly in molecular dynamics simulations. However, for problems in which chain torsions and interchain contacts dominate, use of implicit or United Atoms (UA) may be useful [81]. For example, the concept of United atom model for n-butane is shown in figure 5.1, where each $\text{-CH}_2\text{-}$ and $\text{-CH}_3\text{-}$ group is replaced by a single atom, in such a way that the polymer properties are not changed significantly. The use of UA's can greatly decrease the calculation time. Thus,

- the number of atoms needed in simulation is smaller by a factor of 3,
- the number of non-bonded interactions per atom is also reduced by a factor of 3;
- the time steps can be decreased by a factor of 3 (3 fs for UA simulations compared with 1 fs for all atom simulation).

This leads to a factor of 27 net savings.

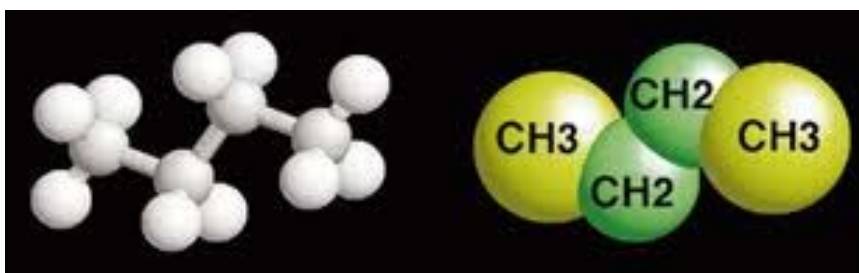


Fig 5.1. Concept of United atoms

5.3 Bead Spring Model

For this work, we considered a bead spring representation [12, 55] of the tethered nano-building blocks that only includes bonds. In this model nanospheres are modeled as spheres of diameters d , permanently connected to tethers via finitely extensible non-linear elastic (FENE) springs. The governing equation for this model is shown in eqn 5.3.1

$$U_{ij}^{\text{FENE}}(r) = -1/2 kR_o^2 \ln[1-(r_{ij}/R_o)^2] \quad (5.3.1)$$

where R_o is the maximum allowable separation and k is the spring constant. The FENE model is very useful to model long-chain polymers. It simplifies the polymers by connecting a sequence of beads with nonlinear springs. Figure 5.2 illustrates the schematic representation of the bead-spring chain model.

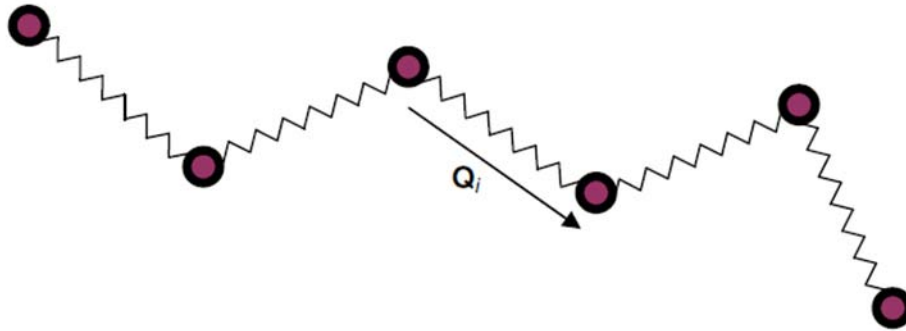


Fig 5.2. Bead-spring chain model with spring configurations given by connector vectors Q_i .

5.4 Simulation Setup

For this work, we consider two different systems (1) a generic model of alkane tethered nanosphere system (i.e., generic Lennard-Jones potential), and (2) alkane tethered amorphous silica nanosphere system. In this study, we treat polymer tethers as n-alkanes, as they are conceptually simple with well-defined interactions, and well-established phase coexistence. In this chapter, the detailed simulation model and methodology of these two systems are presented.

5.4.1 Alkane-Tethered Nanosphere System

Simulation Model

We use a simple model of mono-tethered nanospheres, which is generic enough to be applicable over a wide range of system, but with parameters directly relatable to the physical systems. Our initial studies focus on a CG model of a 1nm nanosphere, with well depth parameters matching that of a buckyball, and nanosphere interactions are modeled with standard 12-6 Lennard-Jones (LJ) potential. The LJ potential is described by

$$U(r) = 4\epsilon \left[\left(\frac{\sigma}{r_{ij}} \right)^{12} - \left(\frac{\sigma}{r_{ij}} \right)^6 \right] \quad (5.4.1)$$

where ϵ is the depth of the potential well, σ is the finite distance at which the inter-particle potential is zero, and r is the center-center distance between the particles.

Nanospheres are modeled as a single site with a spherically symmetric potential. For the results presented in this document, nanospheres are modeled as a Lennard-

Jones sphere with characteristic diameter of nanosphere $\sigma = 9.6 \text{ \AA}$, and the well depth parameter $\varepsilon = 25.3 \text{ kJ/mol}$. This σ parameter was chosen to match the diameter of a C_{60} buckyball, and the effective interaction strength between two buckyballs has $\varepsilon = 25.3 \text{ kJ/mol}$, as calculated from the Girifalco potential [80]. Nanosphere interactions are modeled with “cut and shifted” (CS) LJ potential [23]. In MD simulations, the potential is truncated at the cut-off distance and then shifted with the purpose of eliminating an impulse force at the truncation radius. The so called “cut and shifted” potential takes the form that is shown by

$$U^{cs}(r) = \begin{cases} U(r) - U(r_{cut}), & \text{for } r \leq r_{cut} \\ 0, & \text{for } r > r_{cut} \end{cases} \quad (5.4.2)$$

However, we note that the LJ potential is longer ranged than the Girifalco (GF) potential, which is used to describe interactions between buckyballs, as shown in figure 5.3 (a). Generally, shorter ranged interactions tend to be more characteristic of common silica-based nanoparticles, such as POSS [82]. The formation of coarse-grained nanosphere is also shown in figure 5.3 (b).

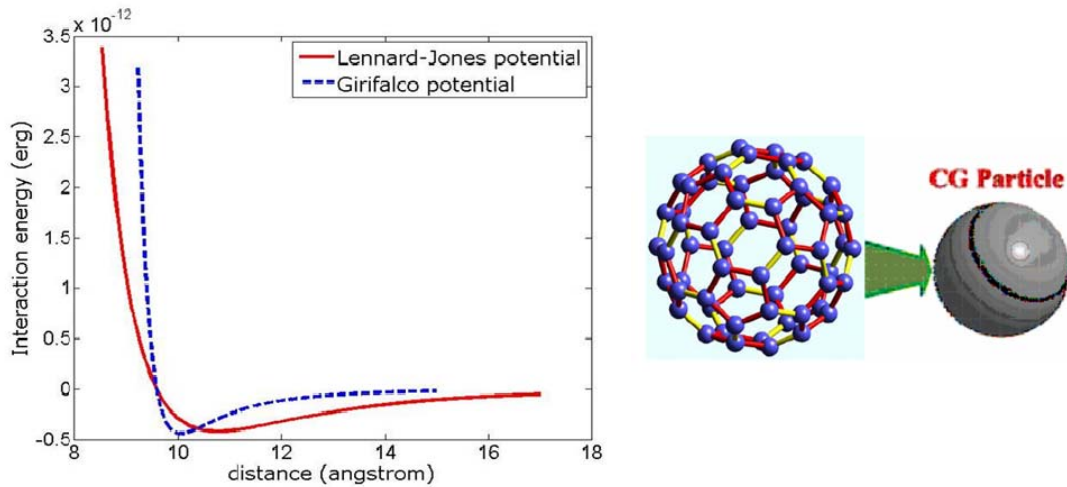


Fig 5.3. (a) Comparison between Lennard-Jones and Girifalco potential, (b) formation of a coarse-grained nanosphere.

5.4.2 Alkane-Tethered Amorphous Silica Nanosphere System

Simulation model

We further extend our work to investigate the phase coexistence behavior of alkane-tethered silica particle system using a CG model of silica. For this system, we perform calculations following the procedure of Lee and Hua [83] to derive effective interaction potentials for amorphous silica nanospheres.

In Lee and Hua's work, a multiscale computational approach to pair potential derivation was proposed, relying on the notion that amorphous silica can be roughly approximated by Si_6O_{12} subunits [83]. They performed atomistic simulations of Si_6O_{12} molecules and used a simplex optimization procedure to derive interaction parameters for CG Si_6O_{12} child particles. The interactions between child particles are approximated by a 12-6 LJ potential. This interaction potential of the CG child particle is used to construct the pair interaction potentials of arbitrary sized and shaped nanoparticles (i.e., larger composite particles were created from the CG'ed child particles). For spherically symmetric nanoparticles, pair potentials were fitted to a 2α - α LJ like form, to ultimately arrive at an effective pair potential for arbitrarily sized spherical silica nanoparticles. However, the results presented in this work appear inconsistent with previous studies of silica nanoparticles [82] with respect to nanoparticle well depth. Specifically, there appears to be a mischaracterization of the strength of epsilon calculated for Si_6O_{12} child particle of diameter 6.2 Å, where the value is off by a factor ~ 4 , as shown in figure 5.4.

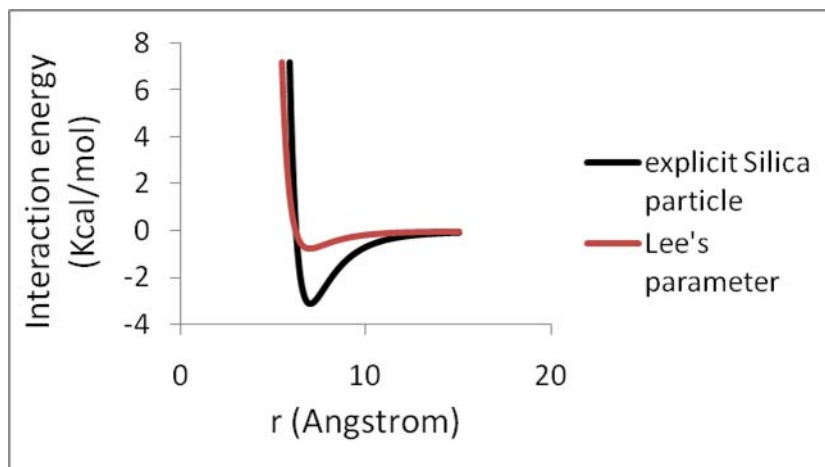


Fig 5.4. Interaction strength comparison between Lee and Hua’s model and explicit Si_6O_{12} system

We determined this was likely a “units” issue, as kJ/mol and Kcal/mol vary by a factor of ~ 4.2 , as other calculations appeared to be correct in a self-consistent manner. Moreover, the fitting equations given in the paper for calculating interaction parameters at different nanoparticle diameters fail to produce accurate results, especially for small nanoparticle sizes, and also fail to reproduce limiting behavior (i.e., the interaction between 0.62 nm particles represented by a single child particle). Because of these shortcomings of Lee and Hua’s work, it is necessary to rederive the pair interaction potentials for the amorphous silica nanosphere systems for small nanosphere diameters of interest.

To rederive parameters, interactions between child particles are given by a 12-6 LJ potential as shown in eqn 5.4.1 and 5.4.2 with $\epsilon = 12.97$ kJ/mol, and $\sigma = 0.62$ nm. We generated nanoparticles by first initializing a bulk system of child particles at density 2.2 gm/cm³.

Then nanoparticles of various sizes are cut from this bulk solution shown in figure 5.5.

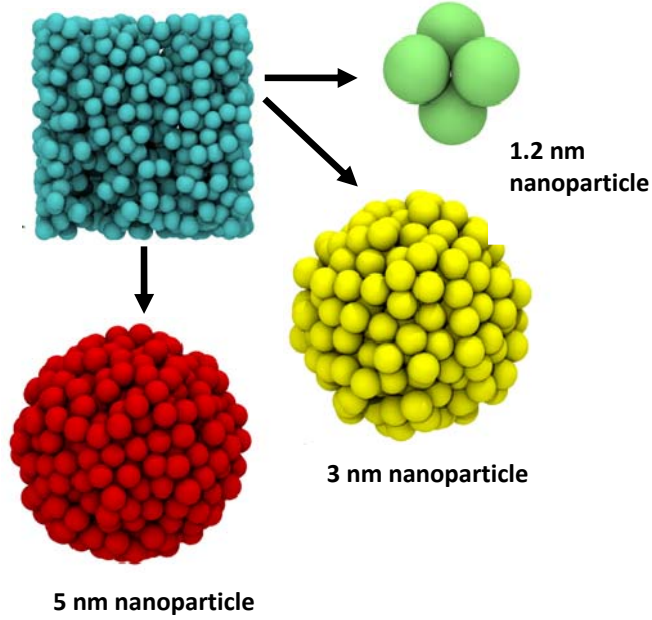


Fig 5.5. Various size spherical nanosphere formation from the bulk system

To calculate the nanoparticle-nanoparticle interactions accurately, the potential energy (U) between two nanoparticles cut from the bulk system is evaluated as a function of separation. This potential is then fitted to the 2α - α LJ functional form.

The functional form of the potential is given by

$$U(r) = 4\epsilon \left[\left(\frac{\sigma}{r_{ij}} \right)^{2\alpha} - \left(\frac{\sigma}{r_{ij}} \right)^\alpha \right] \quad (5.4.3)$$

This procedure is performed for different size nanoparticles to create a plot of interaction parameters of ϵ and α as function of nanoparticle diameter. For example, interaction between 1.2 nm particles is shown in figure 5.6. Figure 5.7 shows the plot of interaction parameters ϵ and α as a function of nanoparticle diameter.

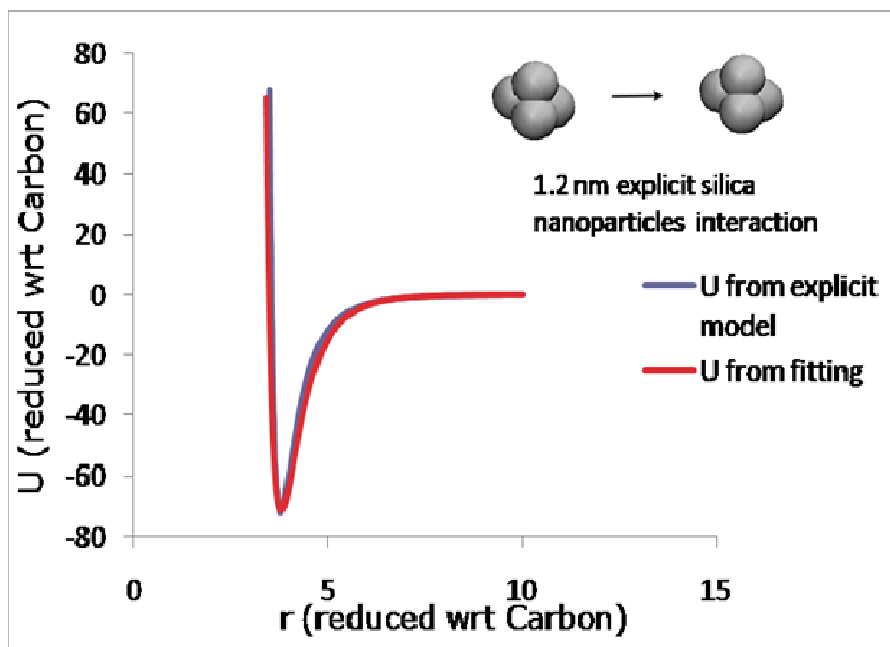


Fig 5.6. Interaction between 1.2 nm silica nanoparticles

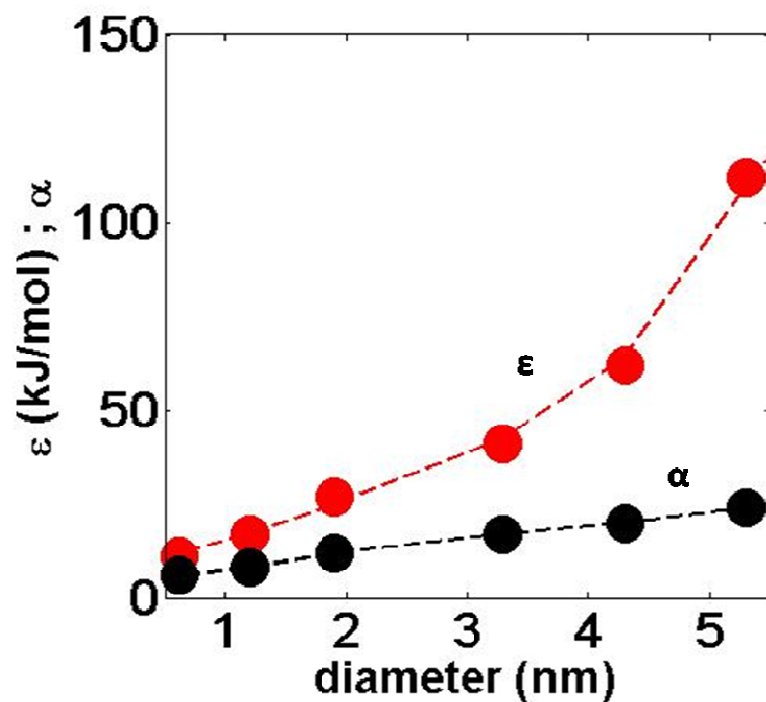


Fig 5.7. Plot of interaction parameters as a function of nanoparticle diameter

Interactions between single-site nanoparticles and polymer beads are calculated by fitting to the potential energy vs separation curve, generated for the interaction between a pseudo-atom and Si_6O_{12} child particle; this fitting is done for each nanoparticle we investigate.

The above mentioned procedure can also be described by using a simple workflow which is shown in figure 5.8.

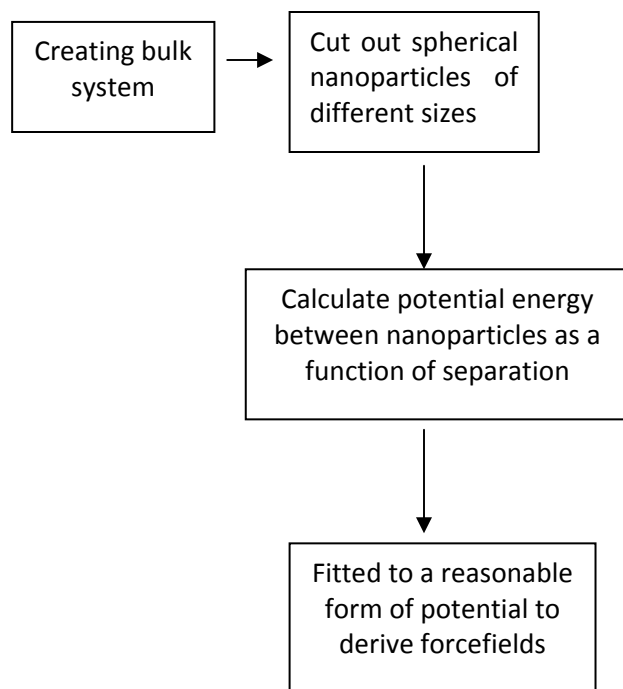


Fig 5.8. Workflow for calculating the interaction potential for the amorphous silica nanoparticle system

For both of these systems, alkane tethers are modeled using a united-atom model, with interactions taken from the TraPPE forcefields for alkyl chains developed by Martin and Siepmann [81]. CH_2 pseudoatoms in the alkyl chain of tether are modeled as Lennard-Jones sphere with $\sigma = 3.95 \text{ \AA}$ and $\epsilon = 0.38 \text{ KJ/mol}$. CH_3 pseudoatom that terminate the tether are also modeled as Lennard-Jones sphere

with $\sigma = 3.75 \text{ \AA}$ and $\epsilon = 0.81 \text{ KJ/mol}$. Cross interactions are calculated using the standard Lorentz-Bertholet mixing rules. The governing equations of Lorentz-Bertholet mixing rule are given by

$$\epsilon_{ij} = \sqrt{\epsilon_i \epsilon_j} \quad (5.4.4)$$

$$\sigma_{ij} = \frac{\sigma_i + \sigma_j}{2} \quad (5.4.5)$$

The bond distance between beads has an equilibrium separation of 1.54 \AA and controlled via a harmonic potential. Note, for simplicity, angle and dihedral terms are neglected and only bead-spring models are considered.

5.5 Simulation Methodology

For both of these models, simulations are performed in the NVT ensemble using the Brownian dynamics thermostat in the GPU enabled HOOMD-Blue [84] simulation package. Simulations are performed with a timestep $\Delta t = 0.235$ femtoseconds. The quench molecular dynamics technique [36] is used for calculating the VLE of these two models. In all cases, potentials are cutoff and shifted to zero at $3.0 \sigma_{ij}$, where σ_{ij} is the characteristic length for the interaction between particles of type i and j .

5.6 Brownian dynamics

Brownian dynamics (BD) [6, 12, 22], a variant of molecular dynamics, is utilized for these simulations. The reason for choosing Brownian dynamics is that it is well known for studying the topological effects of nano-building block geometries.

Furthermore, BD is capable of capturing the appropriate details of the simulations for surfactants, while making the simulations less computationally expensive. The Brownian dynamics (BD) technique is a mesoscopic method in which explicit solvent molecules are replaced instead by a stochastic force. This technique takes advantage of the fact that there is a large separation in time scales between the rapid motion of solvent molecules and the more sluggish motion of polymer or colloids. The ability to coarse-grain out of these fast modes of solvent allows one to simulate much larger time scales than in a standard MD simulation. The BD technique is used to simulate the dynamics of particles that undergo brownian motion. The total force on a particle is composed of a drag force F_i^d from the particle moving through the viscous solvent, a Brownian force F_i^B due to random collision of the solvent with the particle, and all non-hydrodynamic forces F_i^{nh}

$$F_i^{tot} = F_i^d + F_i^B + F_i^{nh} \sim 0 \quad (5.6.1)$$

This total non-hydrodynamic force includes any external body forces, any spring forces and excluded volume interactions. Hydrodynamic drag, including size and shape effects is included through the frictional force, which is given by

$$-\gamma_i \mathbf{v}_i = -6 \pi a \eta \mathbf{v}_i \quad (5.6.2)$$

where γ_i is the friction coefficient, a is the diameter of the atom, η is the solvent viscosity, \mathbf{v}_i is the atom's velocity. Having developed the governing stochastic differential equation, one performs a BD simulation by integrating this equation forward in time. It is necessary to produce many independent trajectories that are averaged together, producing the time evolution of an ensemble-averaged property.

The repetition of many independent trajectories is time consuming but necessary part to follow the time evolution of an averaged property.

5.7 Quench Molecular Dynamics

Vapor-liquid phase coexistence is calculated using the volume-quench dynamics technique [36]. In the quench dynamics method, the system is initialized as a single-phase fluid system with periodic boundary conditions. During the course of the simulation, one dimension of the box is instantaneously expanded and system is equilibrated. The rapid change in density into this unstable region results in the formation of a two-phase system, composed of a well defined liquid region and well defined vapor region. Since the free energy minimization is done by the system through the reduction of the interfacial area, the interfacial region will tend to be planar, allowing us to clearly define the two regions and calculate the density histogram of each of the phases. This procedure is performed several times over a range of temperatures until the vapor and liquid densities of the system become identical or the system attains its critical region. Then a set of VLE data is generated by aggregating the final results. The relationships used to fit the set of VLE data are

$$\frac{1}{2} (\rho_l + \rho_v) = \rho_c + C_1(T - T_c) \quad (5.7.1)$$

$$\rho_l - \rho_v = C_2(T_c - T)^\beta \quad (5.7.2)$$

Here, ρ_l and ρ_v are the liquid and vapor densities respectively, C_1 , C_2 and β are fitting parameters, and ρ_c and T_c are the critical density and critical temperature of the system respectively. By ignoring the interfacial regions between the vapor-liquid

regions, we can calculate the phase coexistence for these complex building blocks in a relatively trivial manner. We found that this methodology is able to reproduce the coexistence behavior of pure LJ fluid with good accuracy. Previous use of this method can also be found in literature where it was used to investigate the saturated liquid densities of the Gaussian charge polarizable water model and the results were found to be matched very closely to those calculated using Gibbs ensemble Monte Carlo simulations and reported in experiment [85]. The schematic representation of the quench dynamics technique is illustrated in figure 5.9.

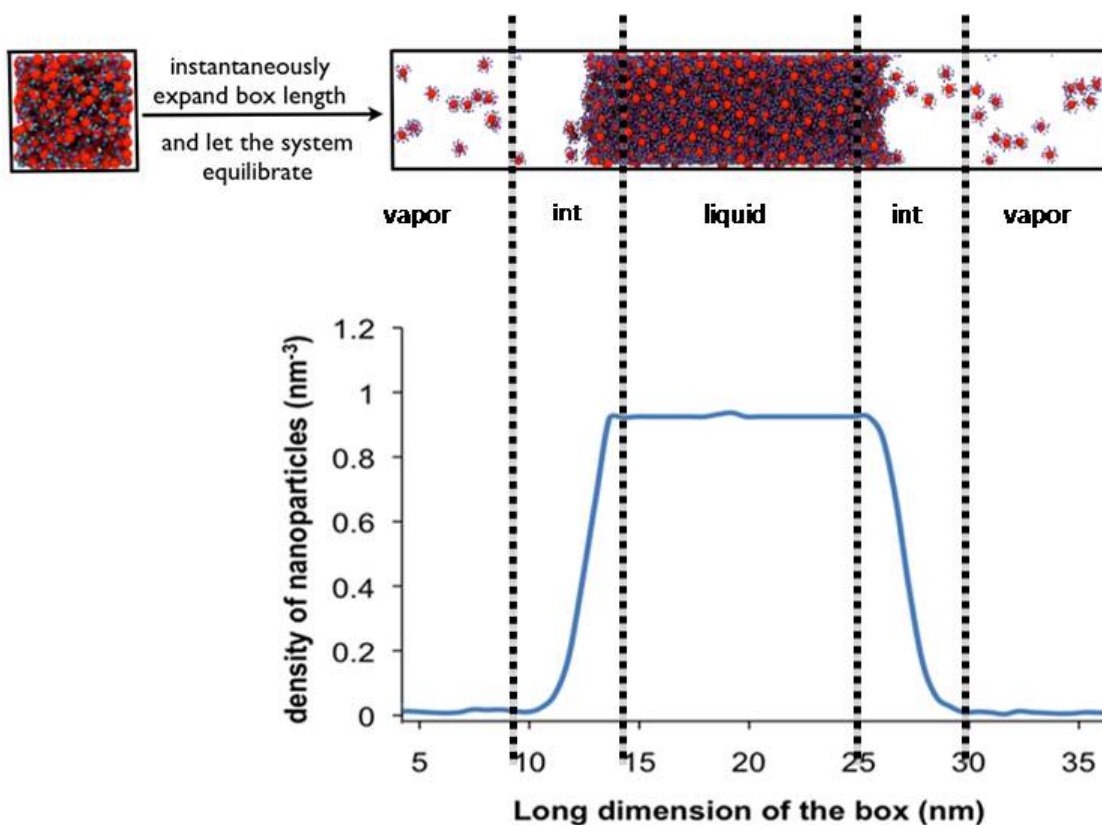


Fig 3. Schematic representation of quench dynamics method

CHAPTER 6

RESULTS & DISCUSSIONS

6.1 Alkane-Tethered Nanosphere System

For this system vapor-liquid equilibrium (VLE) is calculated as a function of tether length, and interaction strength between nanospheres. The simulation results are then compared with SAFT-VR equation of state [86] results. For all of the simulation calculations performed for this system, alkane-tethers are considered to be freely moving on the surface of the nanoparticles.

6.1.1 VLE As a Function of Chain Length

First, we investigated VLE as a function of tether length. Figure 6.2 shows the VLE of mono-tethered nanosphere system ($n_{\text{chain}}=1$) at varying tether lengths, starting from bare nanoparticle system and then increasing the length of the tether with $n_{\text{totalbeads}}=4$, $n_{\text{totalbeads}}=8$ and $n_{\text{totalbeads}}=12$. The schematic representations of these systems are shown in figure 6.1.

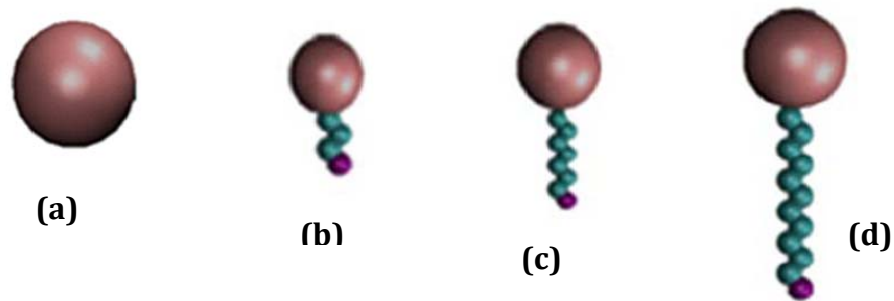


Fig 6.1. Schematic representation of different systems considered for VLE calculation. (a) bare nanoparticle, (b) mono-tethered nanosphere ($n_{\text{totalbeads}}=4$), (c) mono-tethered nanosphere ($n_{\text{totalbeads}}=8$), (d) mono-tethered nanosphere ($n_{\text{totalbeads}}=12$)

We predict from figure 6.2 that, with the increase in the tether length, the critical temperature of the system decreases. The tethers sterically restrict the structural aggregation of the nanoparticles, effectively shielding the strong interactions, resulting in a decrease in overall critical temperature of the system.

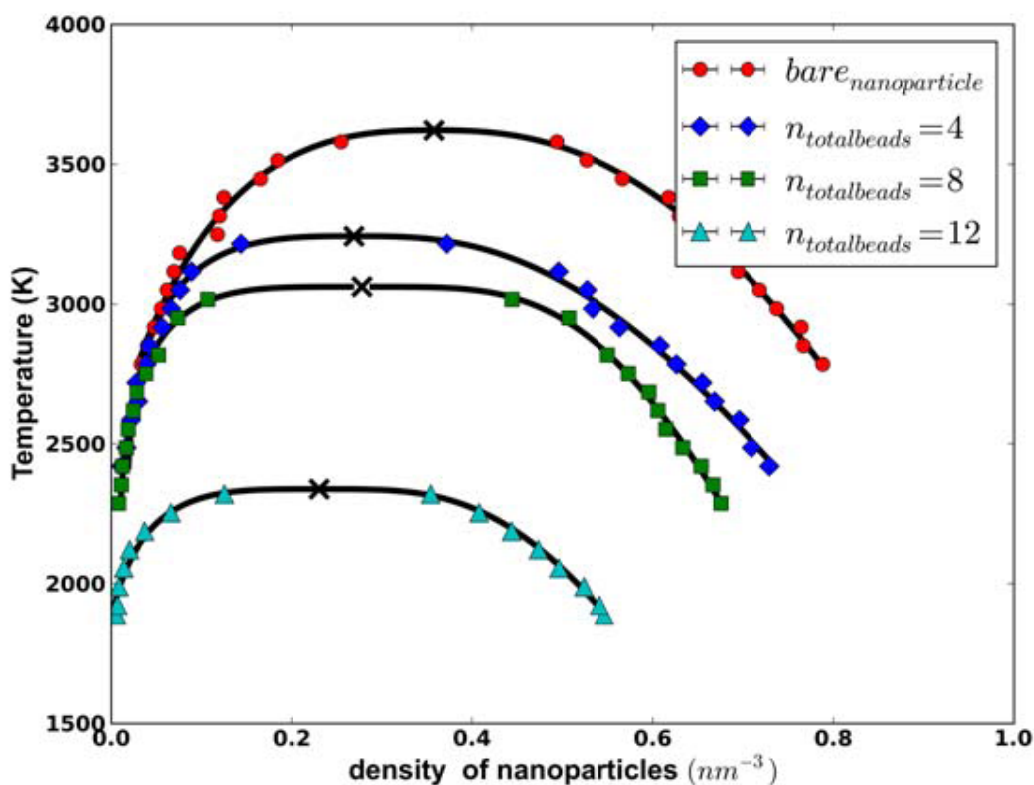


Fig 6.2. VLE of mono-tethered nanosphere system ($n_{chain}=1$) at different tether lengths. Symbols represent simulation results and lines represent prediction using both rectilinear and scaling laws. The critical temperature is represented by (\times) symbol.

This decreasing trend in critical temperature with the increase in tether length is the inverse of what is typically seen for pure alkane fluids, where the critical temperature of the system increases with the increase in the number of carbon atoms in the alkane chain [35, 81]. This behavior can be understood more clearly from figure 6.3.

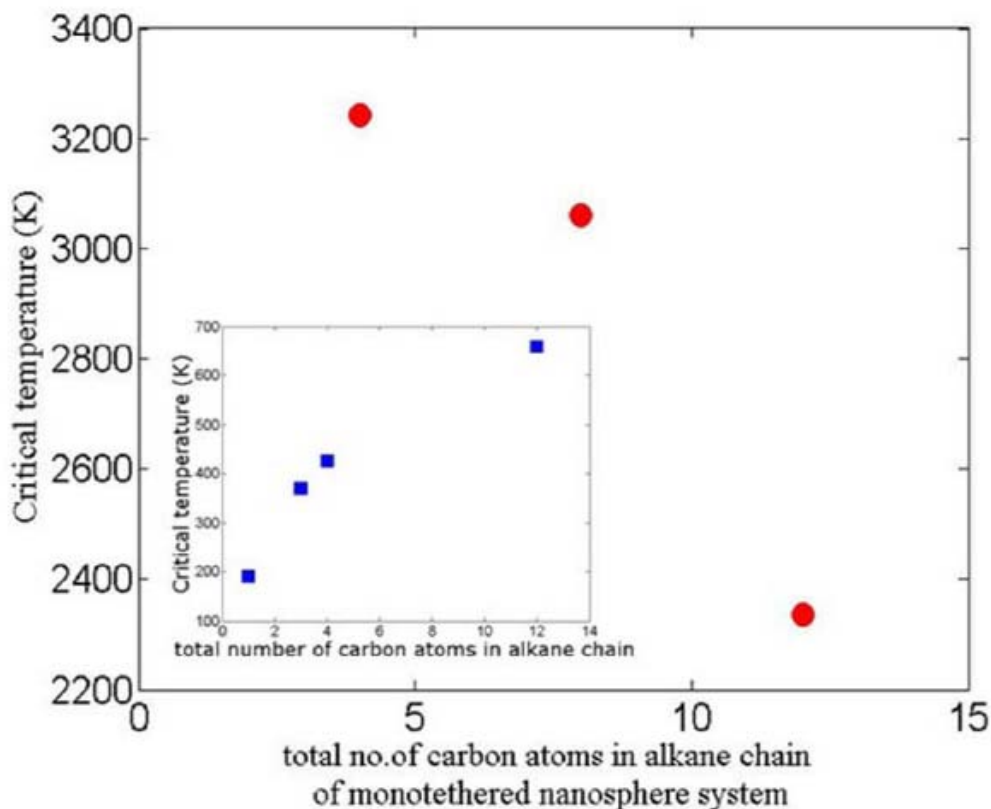


Fig 6.3. Plot of critical temperature as a function of tether length for alkane-tethered nanosphere system. Plot of critical temperature for normal alkanes is shown in the inset.

6.1.2 VLE As a Function of Interaction Strength

For this system, VLE is also calculated as a function of nanoparticle interaction strength. The interaction strength is varied with $\epsilon = 2.76$ and 25.3 kJ/mol. Figure 6.4 shows the phase behavior of mono-tethered nanosphere ($n_{\text{chain}}=1$, $n_{\text{totalbeads}}=12$) system as a function nanoparticle interaction strength. The critical temperature of the system is directly proportional to the interaction strength, i.e. with the increase in the strength of interaction the critical temperature of the system will always increase as nanoparticle-nanoparticle interaction is the strongest interaction in the system.

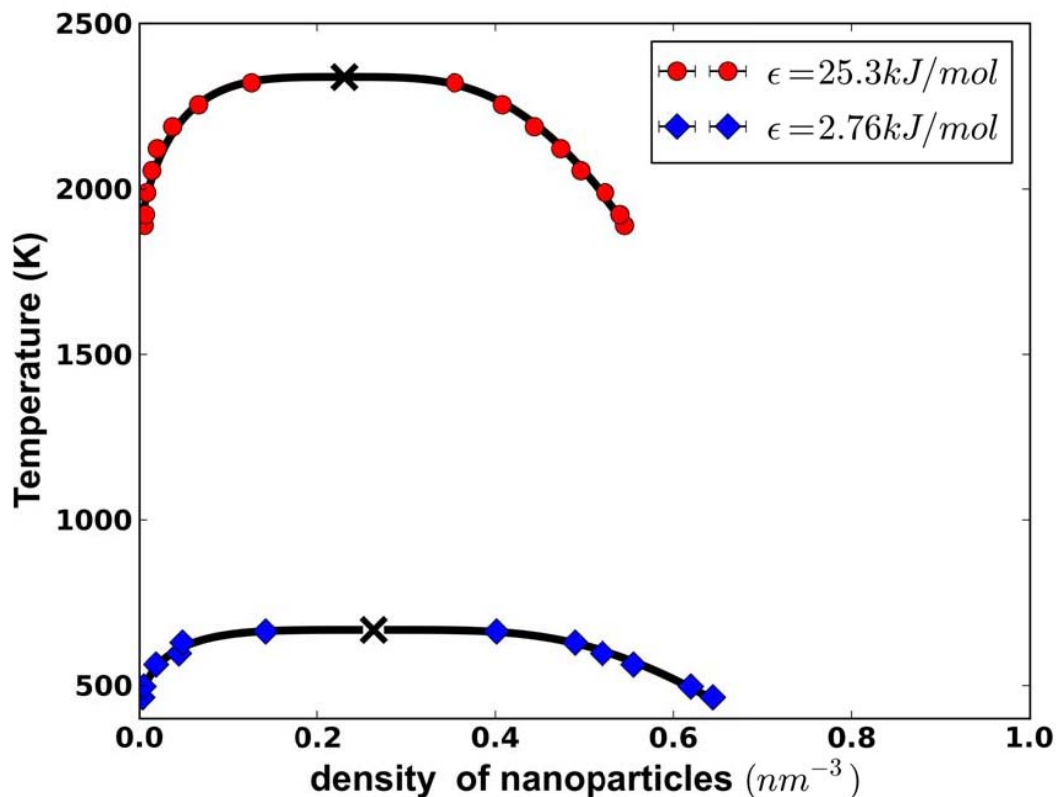


Fig 6.4. Phase behavior of mono-tethered nanosphere ($n_{totalbeads} = 12$) system at different nanoparticle interaction strength. Symbols represent simulation results and lines represent prediction using both rectilinear and scaling laws. The critical temperature is represented by (\times) symbol.

6.1.3 Comparison With SAFT-VR Equation of State

We also compared our VLE results of the alkane-tethered nanosphere system to calculations performed using SAFT-VR. The primary reason for considering SAFT-VR is SAFT can easily calculate the VLE of larger diameter nanoparticles or longer polymers, which is not trivial in simulation. The SAFT-VR calculations were carried out by Jessica Haley in the group of our theoretical collaborator (Dr. Clare McCabe). For the initial comparison, SAFT-VR parameters are derived by fitting to simulation isotherms, following the procedure outlined by Peng & McCabe in ref. [86]. Figure

6.5 shows comparison of the vapor-liquid VLE behavior of a 12 bead mono-tethered nanosphere system with simulation and SAFT-VR equation of state.

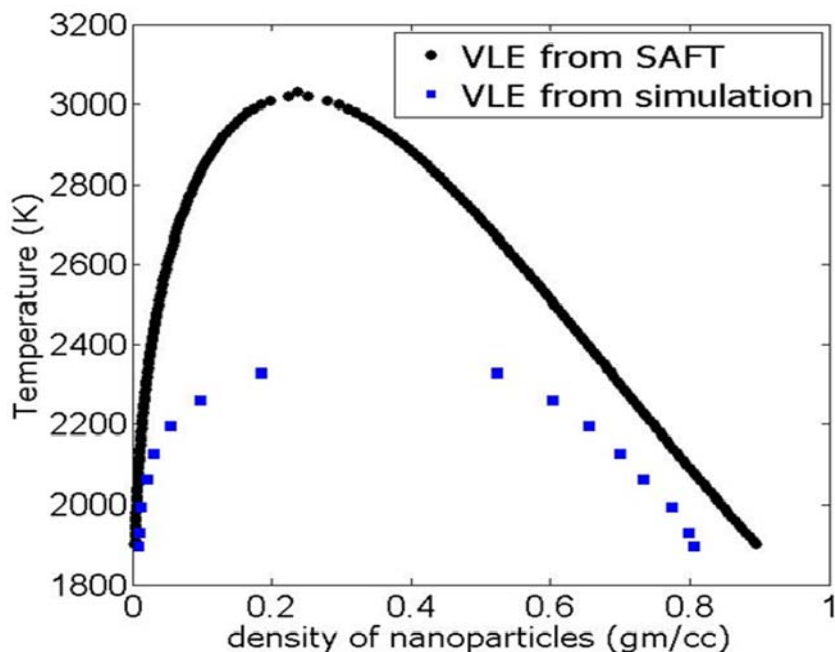


Fig 6.5. VLE of mono-tethered nanosphere system with simulation (■) and SAFT-VR (●)

Although SAFT-VR is able to capture the similar coexistence envelope compare to simulation in terms of density, the critical temperature of the system predicted by SAFT-VR is higher than the simulation calculation. This is expected because SAFT exhibits classical behavior in the critical region rather than the nonanalytical, singular behavior seen in real systems [87]. As a result, accurate agreement over the whole phase diagram cannot be obtained. Figure 6.6 shows the pressure-density isotherm comparison between simulation and SAFT-VR, used to fit these parameters, where it can be seen from this figure that our simulation results fitted reasonably well with the theoretical prediction.

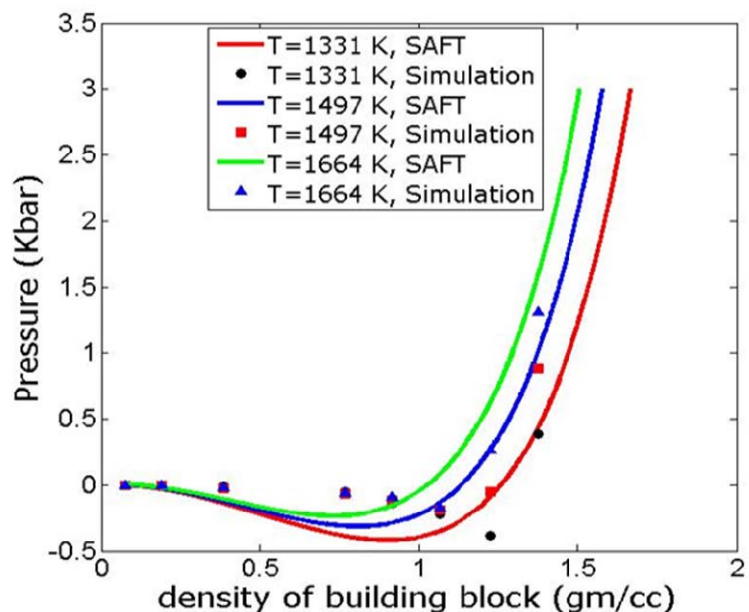


Fig 6.6. Pressure density isotherms of mono-tethered nanosphere system using SAFT-VR (solid lines) and simulation (symbols)

Figure 6.7 shows the VLE of tethered nanosphere system as a function of tether length using SAFT-VR, where we observed obvious similar trends to those previously observed trend in figure 6.2 and 6.3, namely a decrease in critical temperature with increasing tether length.

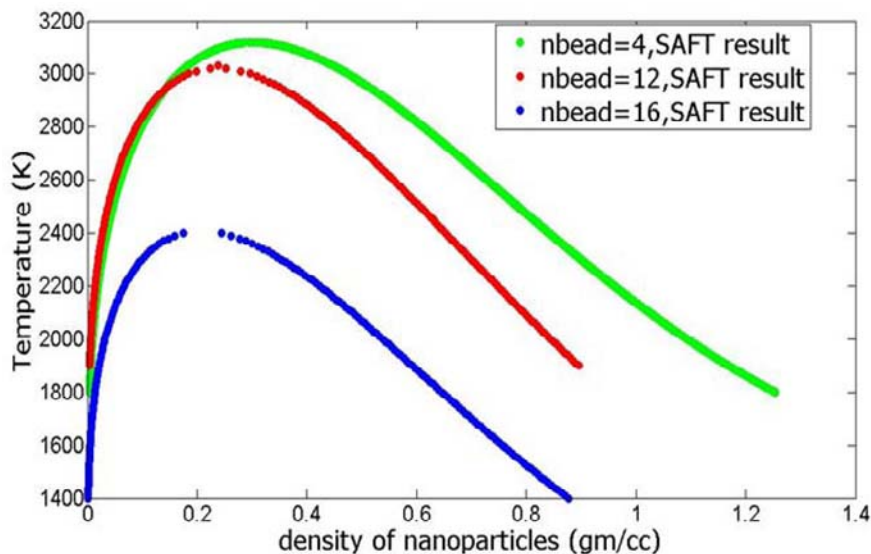


Fig 6.7. VLE of mono-tethered nanosphere system using SAFT-VR theory at different tether lengths

6.2 Alkane-Tethered Amorphous Silica Nanosphere System

For this system, vapor-liquid equilibrium (VLE) behavior is investigated for two different cases- (1) tethers are free to move on the surface of the nanoparticles, and (2) tethers are fixed at the surface of the nanoparticles at specific angles. For case (1), the VLE is calculated as a function of system size, as a function of number of chains, as a function of chain length and as a function of nanoparticle diameter. The schematic representation of the tethered silica nanosphere system at different anisotropic conditions is shown in figure 6.8.

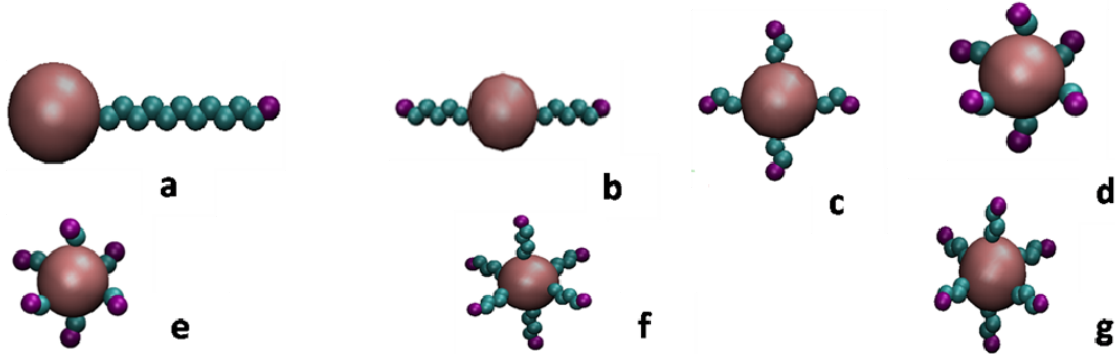


Fig 6.8. Schematic representation of tethered silica nanoparticle system at different anisotropic conditions, (a) mono-tethered, (b) di-tethered, (c) quad tethered, (d) hexa-tethered, (e), (f), and (g) variation of the tether lengths

For case (2), VLE is calculated for di-tethered system with nanoparticle diameter of $D = 0.62$ nm, where, the lengths of the two tethers are fixed at 6 beads each. A harmonic spring is used to control the planar angle, θ , between tethers at the nanoparticle surface. Here, VLE is investigated as a function of planar angle, θ , which is fixed at 60° , 90° , 120° and 180° .

6.2.1 VLE As a Function of System Size (Tethers are free to move)

First we calculate the VLE of TNP system as a function of system size to determine the minimum size needed to produce clear vapor and liquid phases. For this calculation, we have considered a di-tethered system ($n_{chain} = 2$) of nanoparticle diameter $D = 0.62$ nm and with a total number of 12 polymer beads ($n_{totalbeads} = 12$) attached to it. Calculations are performed with 500, 1000, and 1500 building-blocks (BBs), where the initial single phase box ratios are given as 1:1:1, 2:1:1, and 3:1:1 respectively. Fig 6.9. shows the VLE behavior of TNP system as a function of the number of BBs.

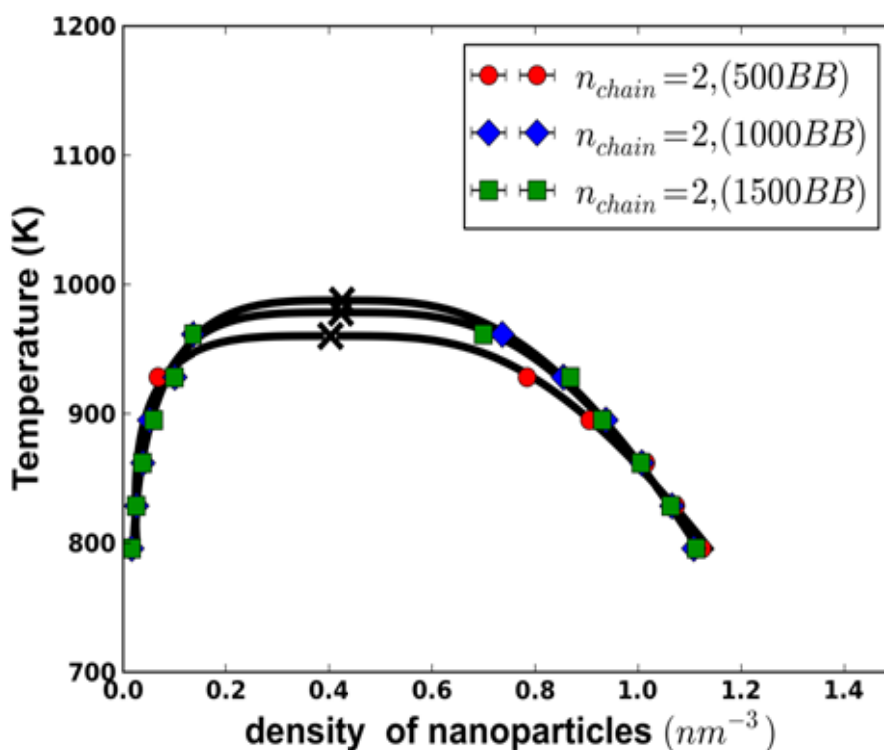


Fig 6.9. VLE of alkane-tethered silica nanoparticle system as a function of system size. Symbols represent simulation results and lines represent prediction using both rectilinear and scaling laws. The critical temperature is represented by (\times) symbol.

While all phase tend to produce similar results, system composed of 1000 and 1500 BBs are nearly identical and both provide clearly identifiable vapor, liquid, and interfacial regions. For systems composed of 500 BBs, the interfacial region tends to dominate, obscuring a clear picture of the liquid phase. As such, calculations of 1000 BBs are utilized through the rest of this work.

6.2.2 VLE As a Function of Number of Chains (Tethers are free to move)

We investigate the effect of the number of chains (n_{chain}) on the VLE, where the total number of chain beads are kept fixed at $n_{\text{totalbeads}} = 12$ for nanoparticle diameter $D = 0.62$ nm. As such, $n_{\text{chain}} = 1$ has a single 12-bead polymer chain attached to it, and $n_{\text{chain}} = 2, 4, 6$ have 6, 3, 2-bead polymer chains attached to the surface respectively. Note, in these simulations, chains are free to move about the surface. From figure 6.10 we found that the critical temperature of the system decreases as the number of chains increases, but the critical density of the systems remains almost unaffected. We also calculated the potential of mean force (PMF) between nanoparticles in vapor phase to understand this behavior and to reinforce our observations. The plot of potential of mean force as a function of no. of chains is shown in figure 6.11.

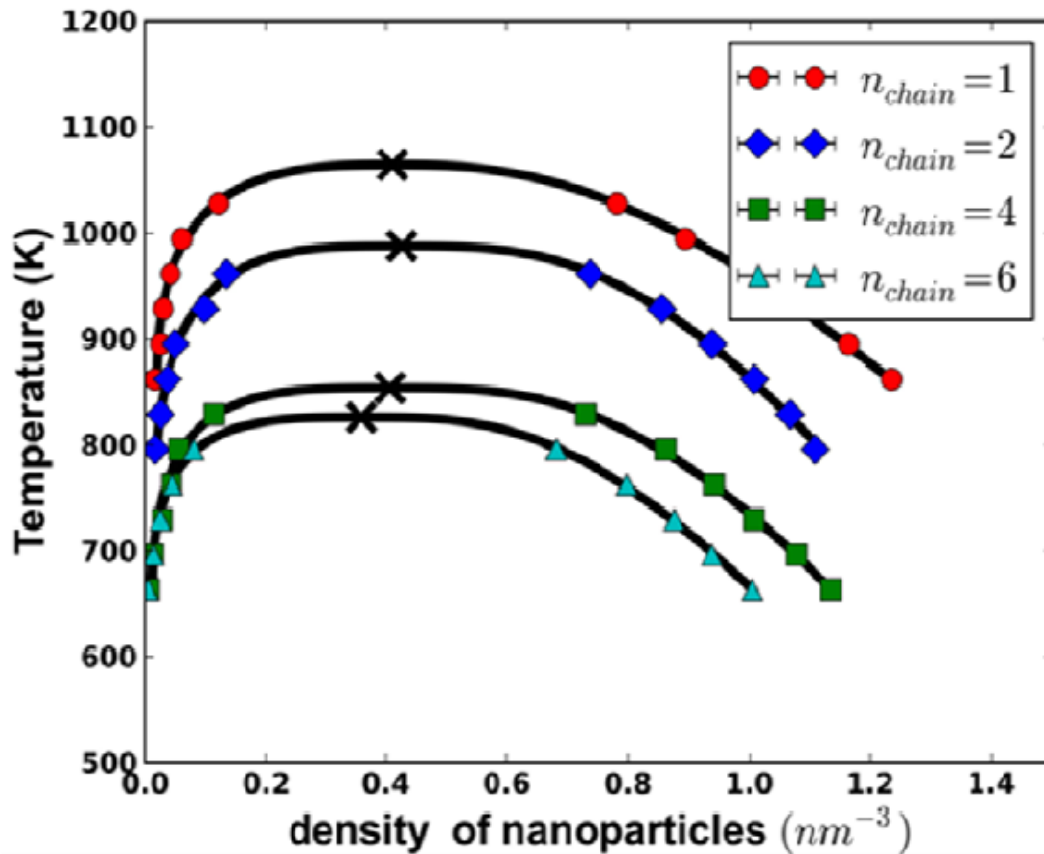


Fig 6.10. VLE of alkane-tethered silica nanoparticle system as a function of number of chains. Symbols represent simulation results and lines represent prediction using both rectilinear and scaling laws. The critical temperature is represented by (\times) symbol.

For both mono-tethered ($n_{chain} = 1$) and di-tethered ($n_{chain} = 2$) systems, an effective attractive interaction regions between nanoparticles is found, but such behavior is not observed for higher number of grafts. As the number of tethers is increased, the accessible surface area of the nanoparticle is decreased, prohibiting the nanoparticles from strongly interacting. For hexa-tethered ($n_{chain} = 6$) system this behavior is most prominent and a clear repulsive region is observed corresponding to the steric interactions of the polymer coating. Furthermore, as the number of grafts increases, the critical temperatures shifts towards that of the bulk alkane (T_c

~ 670 K), further indicating that the phase behavior is increasingly dictated by the polymer-polymer interactions rather than strong nanoparticle-nanoparticle interactions.

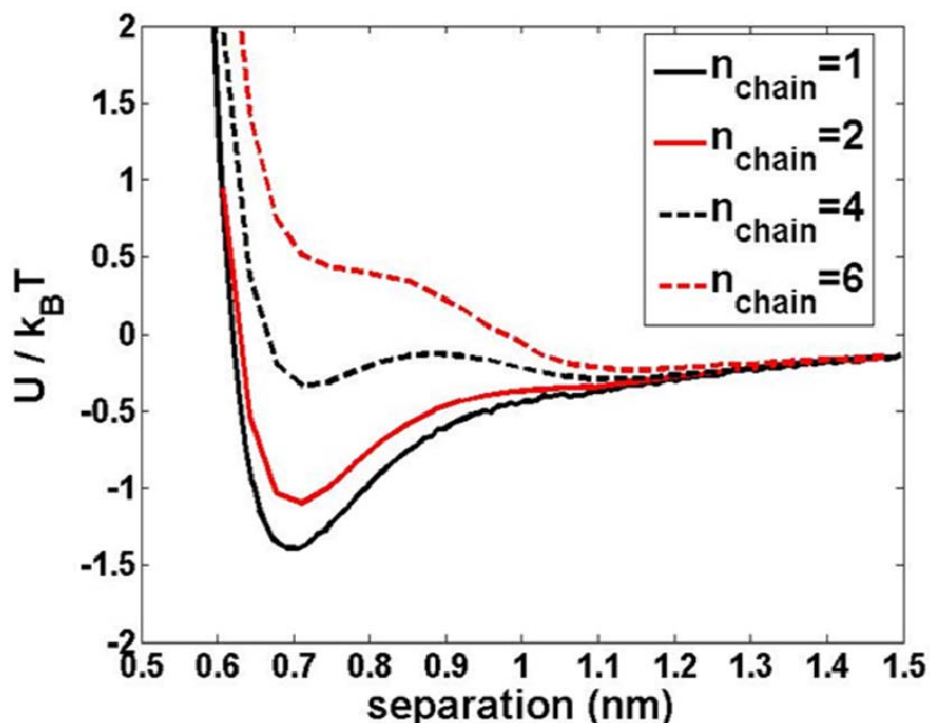


Fig 6.11. Potential of mean force (PMF) between nanoparticle centers as a function of number of chains.

6.2.3 VLE As a Function of Chain Length (Tethers are free to move)

We then investigated the VLE of the alkane-tethered silica nanoparticle system as a function of tether length with nanoparticle diameter $D = 0.62$ nm. Figure 6.12, 6.13, and 6.14 represent the VLE of di-tethered ($n_{\text{chain}}=2$), quad-tethered ($n_{\text{chain}}=4$) and hexa-tethered ($n_{\text{chain}}=6$) systems at various tether lengths. For example, for di-tethered system ($n_{\text{chain}}=2$), $n_{\text{totalbeads}} = 12$ corresponds to a system where the lengths of the two tethers are fixed at 6 beads each whereas, $n_{\text{totalbeads}} = 24$ corresponds to a system where the lengths of the two tethers are fixed at 12 beads each. For quad-

tethered system ($n_{\text{chain}}=4$), $n_{\text{totalbeads}} = 12$ corresponds to a system where the lengths of the four tethers are fixed at 3 beads each but $n_{\text{totalbeads}} = 32$ corresponds to a system where the lengths of the four tethers are fixed at 8 beads each. Similar analogy can be applied for the hexa-tethered ($n_{\text{chain}}=6$) system also, where $n_{\text{totalbeads}} = 30$ corresponds to a system where the lengths of the six tethers are fixed at 5 beads each. From figure 6.12, 6.13 and 6.14 it can be seen that as the length of the tether increases, the overall critical temperature decreases for each systems and as also the critical density. The tethers sterically restrict the structural aggregation of the nanoparticles, effectively shielding the strong interactions, resulting in a decrease in overall critical temperature of the system. Peng and McCabe calculated the VLE of tethered polyhedral oligomeric silsesquioxane (POSS) nanocubes as a function of tether chain lengths using the hetero-SAFT-VR approach [86] and found similar behavior to that observed in our study, where there is a decrease in critical temperature with the increase in grafting length. This behavior of decreasing critical temperature is the inverse of what is typically seen in pure alkane fluids, where critical temperature increases with the increase in chain length [35, 81] .

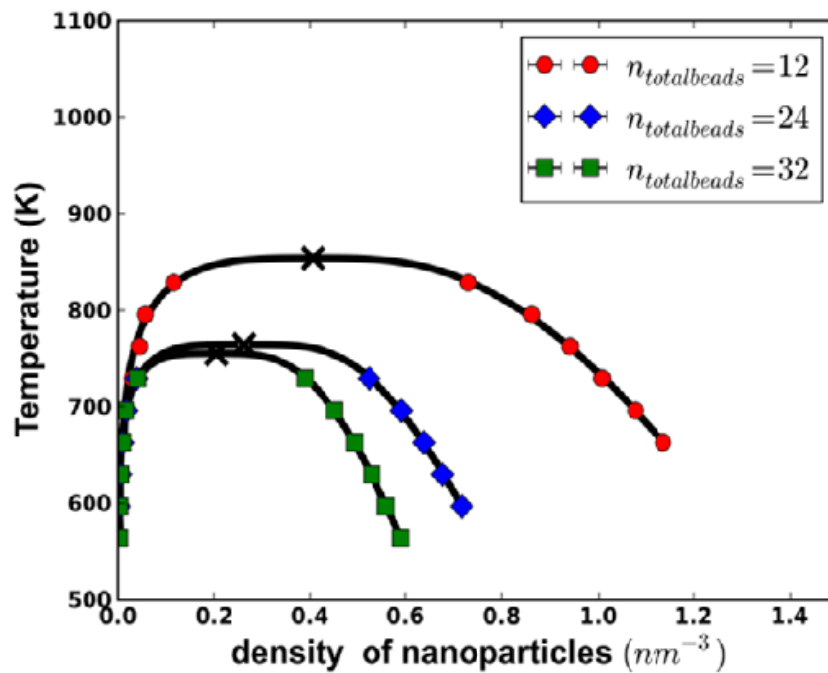
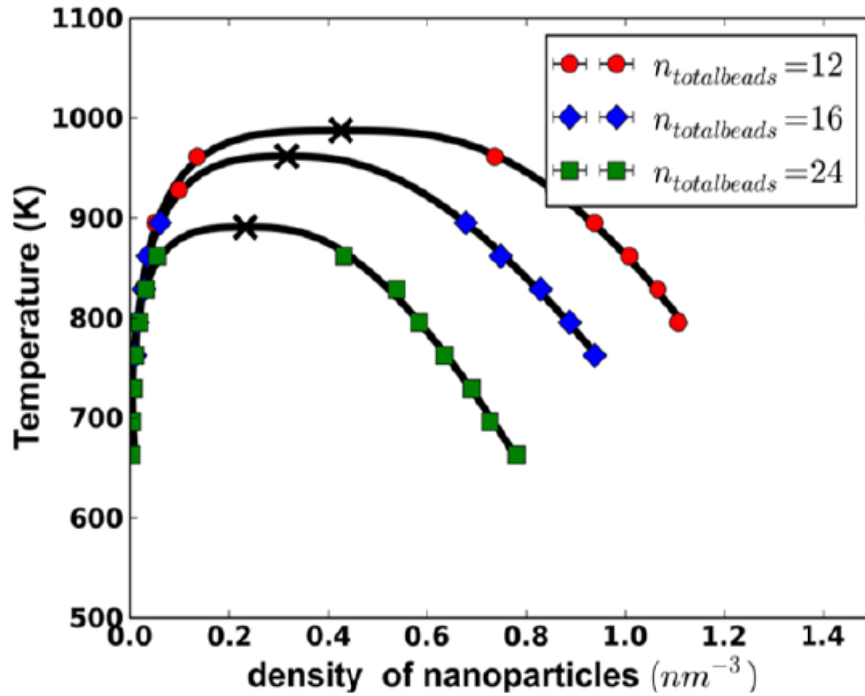


Fig 6.12. VLE of di-tethered ($n_{chain}=2$) silica nanoparticle system at different tether lengths. **Fig 6.13.** VLE of quad-tethered ($n_{chain}=4$) silica nanoparticle system at different tether lengths. Symbols represent simulation results and lines represent prediction using both rectilinear and scaling laws. The critical temperature is represented by (\times) symbol.

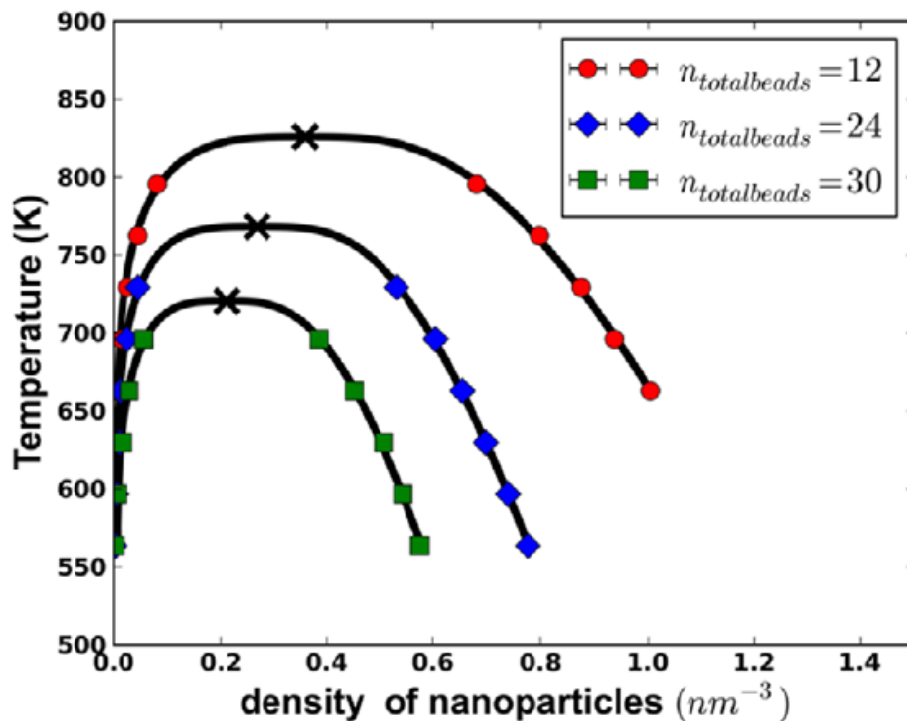


Fig 6.14. VLE of hexa-tethered ($n_{chain}=6$) silica nanoparticle system at different tether lengths. Symbols represent simulation results and lines represent prediction using both rectilinear and scaling laws. The critical temperature is represented by (\times) symbol.

6.2.4 VLE as a function of nanosphere diameter (Tethers are free to move)

We also investigated the VLE of hexa-tethered ($n_{chain}=6$) system as a function of nanoparticle diameter. For this calculation, the total number of chain beads are kept fixed with $n_{totalbeads}=12$ and the diameters of the nanoparticles considered are $D = 0.62$ nm and 1.2 nm. Figure 6.15 represents the phase behavior of hexa-tethered silica nanoparticle system ($n_{chain}=6$) as a function of nanoparticle diameter. A significant increase in the overall critical temperature of the system can be seen with the increase in nanoparticle diameter. The significant increase in nanoparticle-nanoparticle interaction combined with the increased surface area is the primary cause of the increased critical temperature. Additionally, from this plot, we see an

increase in the volume fraction as the nanoparticle diameter is increased. The relative interaction range is reduced as nanoparticle diameter is increased, requiring higher densities for fluid phases for larger diameter nanospheres (1.2 nm in this case).

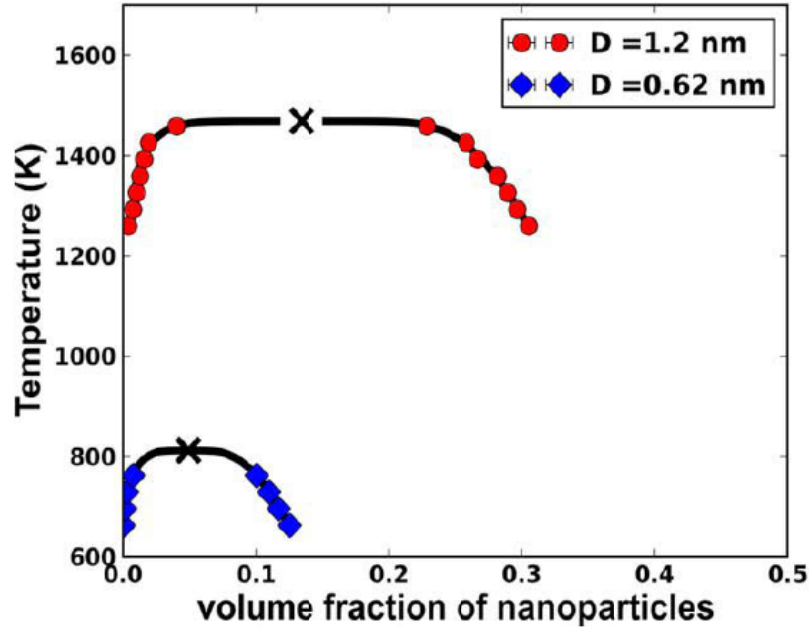


Fig 6.15. VLE of hexa-tethered ($n_{\text{chain}}=6$) silica nanoparticle system at different nanoparticle diameters. Symbols represent simulation results and lines represent prediction using both rectilinear and scaling laws. The critical temperature is represented by (\times) symbol.

We then decided to calculate the phase behavior of these two different diameter tethered silica nanosphere systems (namely $D = 0.62$ nm, and $D = 1.2$ nm) by conserving the total number of tether chains (n_{chain}) to the surface area of nanosphere (SA) ratio for both the systems. The main purpose of the calculation was to shield most of the strong nanoparticle-nanoparticle interactions for 1.2 nm system. This strong nanoparticle interaction resulted in a significantly higher critical temperature for 1.2 nm system compared to the 0.62 nm system at same conditions

i.e $n_{chain} = 6$, and $n_{totalbeads}=12$, which is demonstrated in figure 6.15. For this calculation, the total number of chains (n_{chain}) considered is 6, giving a value of $n_{chain}/SA \sim 4.97$ chains/nm² for a 0.62 nm particle. For 1.2 nm particle, to conserve this value of 4.97 chains/nm², total 24 number of tether chains needs to be attached. A tethered silica nanosphere system is then generated with $n_{chain}=24$, and $n_{totalbeads}=48$ and the phase behavior of this system is investigated. Figure 6.16 shows the VLE of 0.62 and 1.2 nm tethered nanosphere systems by conserving the ratio of total number of tether chains (n_{chain}) to the surface area of nanosphere (SA) i.e n_{chain}/SA between these two systems.

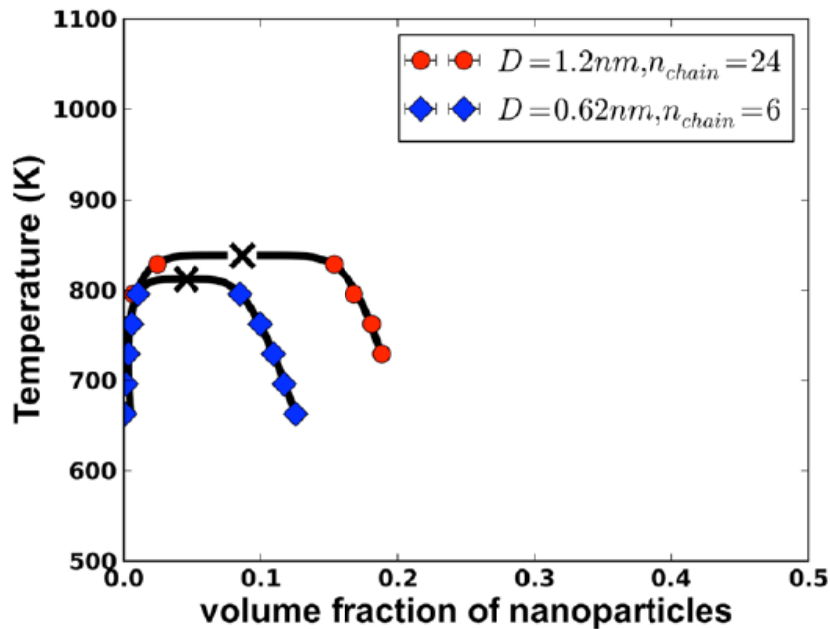


Fig 6.16. VLE of hexa-tethered silica nanoparticle system by conserving the n_{chains}/SA ratio. Symbols represent simulation results and lines represent prediction using both rectilinear and scaling laws. The critical temperature is represented by (\times) symbol.

From figure 6.16 it can be predicted that the critical temperature of 1.2 nm system decreased significantly compared to figure 6.15 and it now matches quite closely

with the critical temperature of 0.62 nm system. The increase in the total number of tethers attached to the nanoparticle ($n_{\text{chain}} = 24$) for 1.2 nm tethered nanosphere system actually resulted in the decrease in the accessible surface area of the nanoparticle. Thus the tethers prohibit the nanoparticles from strongly interacting which causes in the overall decrease of critical temperature for 1.2 nm system.

6.2.5 VLE As a Function of Planar Angle (θ) Between Tethers (Fixed Tethers)

We also determined VLE of this system as a function of planar angle (θ) between tethers at the nanoparticle surface. A harmonic spring is used to control the planar angle, θ , between tethers at the nanoparticle surface. For this investigation, VLE is calculated for di-tethered ($n_{\text{chain}} = 2$) system with nanoparticle diameter of $D = 0.62$ nm, where, the lengths of the two tethers are fixed at 6 beads each. The schematic representation of the model di-tethered system is shown below in figure 6.17.

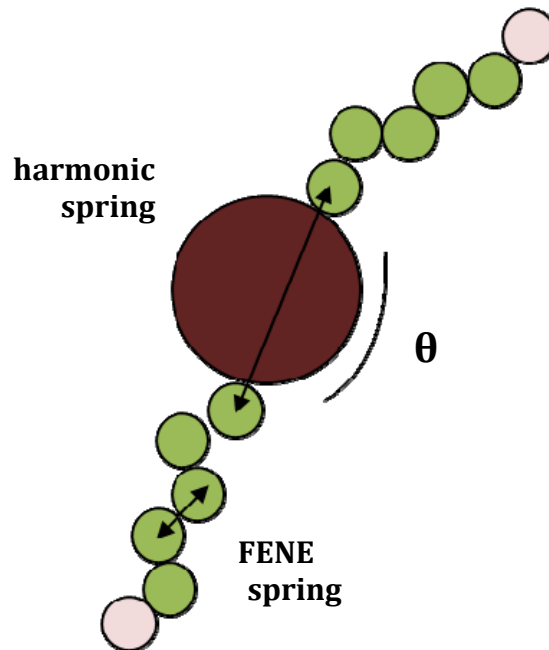


Fig 6.17. Schematic representation of the model di-tethered silica nanoparticle system with fixed tethers

For this case, VLE is explored as a function of planar angle, θ , which is fixed at 60° , 90° , 120° and 180° . The histogram of the distribution of the angle (for 60°) is shown in figure 6.18. The histogram represents a Gaussian distribution with an average angle of 60° and a standard deviation of ~ 3 . So, it can be said that the harmonic spring can be used effectively to fix the position of the tethers at the surface of the nanoparticle.

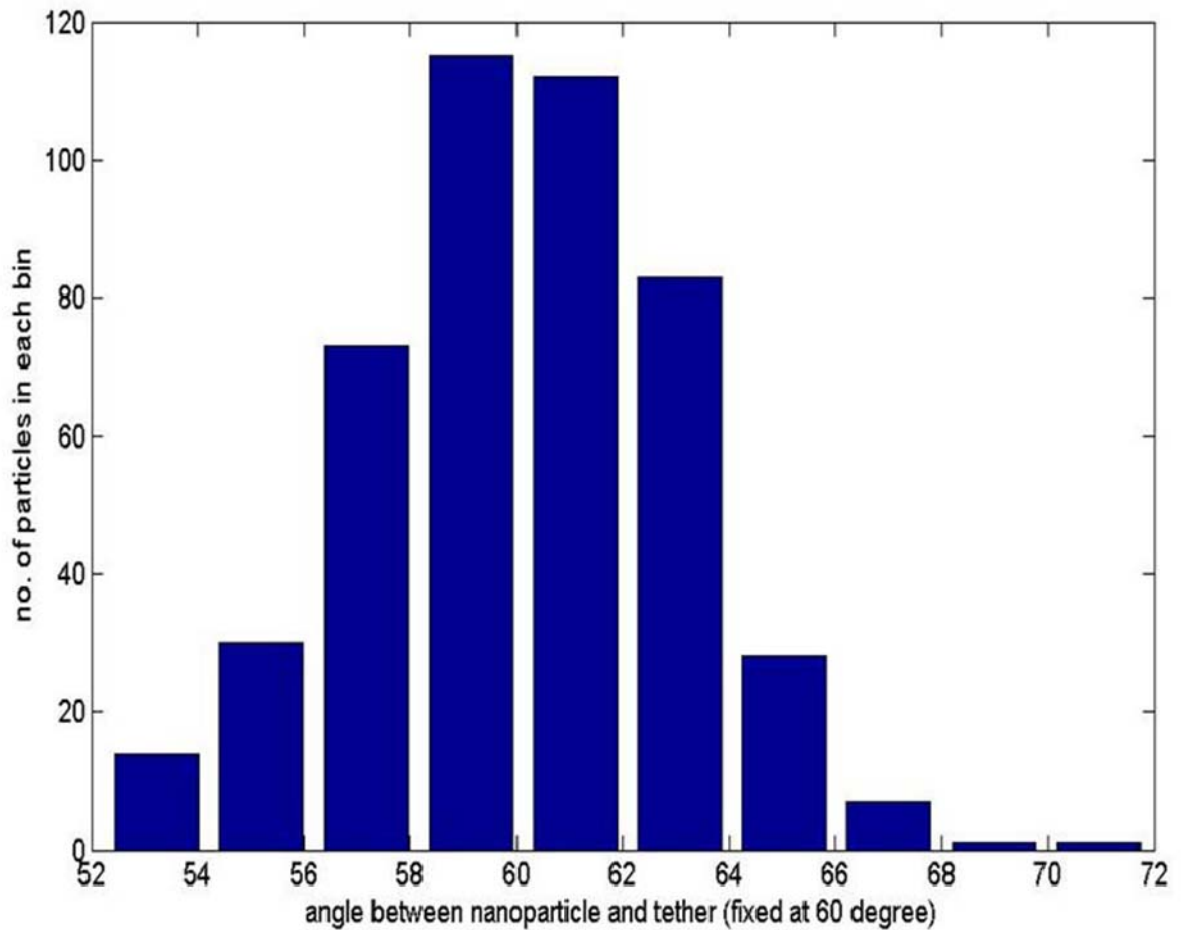


Fig 6.18. Histogram of the distribution of the planar angle (θ) between tethers at the nanoparticle surface. In this case, the tethers are fixed at 60°

The plot of VLE as a function of planar angle (θ) is shown in figure 6.19. A steadily decreasing trend in critical temperature with the increase in the angle from 60° - 180° can be seen from the figure. At 60° , the tethers are distributed mostly at one side on the surface of the nanoparticle, for that reason, polymers could not screen the strong nanoparticle interactions effectively, resulting in a higher critical temperature of the system. But with the increase in the planar angle (θ), effective screening of nanoparticle interactions are done and with the planar angle of 180° , most of the interactions are screened because of the equal distribution of polymers at the surface of the nanoparticle which results in a clear decrease in the critical temperature of the system.

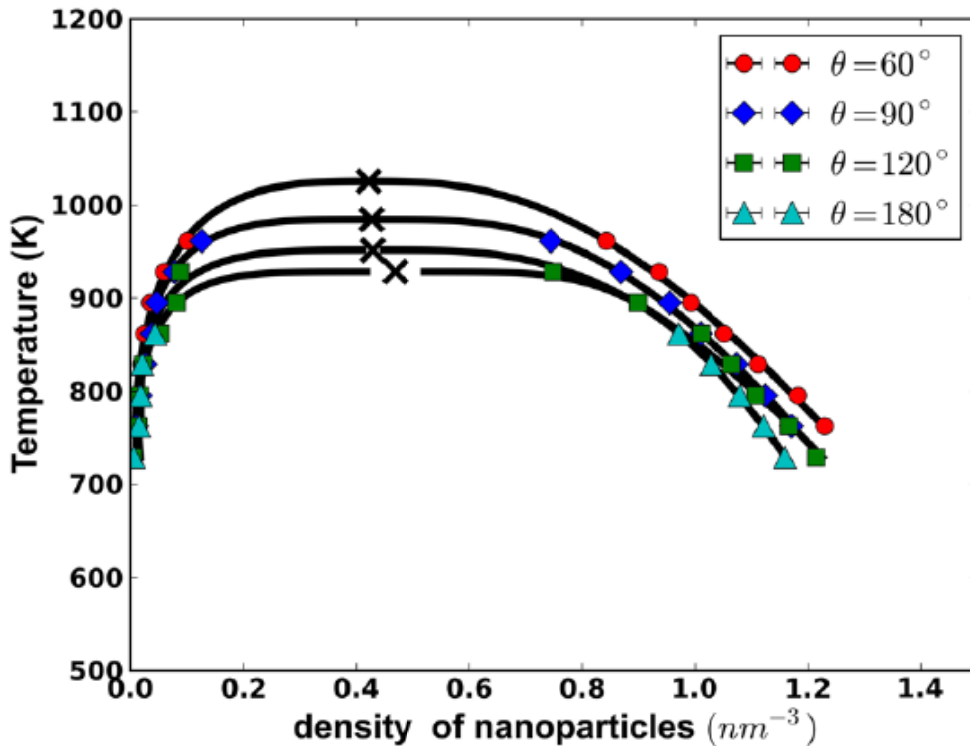


Fig 6.19. VLE of di-tethered ($n_{\text{chain}}=2$) silica nanoparticle system as a function of planar angle (θ) between tethers at the nanoparticle surface. Symbols represent simulation results and lines represent prediction using both rectilinear and scaling laws. The critical temperature is represented by (\times) symbol.

6.2.6 Accuracy Test of the Estimated Critical Temperatures (T_c)

For all the VLE calculations shown in this work, the critical temperatures of different systems are calculated using the fitting equations given in equation 5.7.1 and 5.7.2. But there could be some approximations of the calculated critical temperatures of the systems as the fitting provided by these equations might not be exactly accurate. We came up with a procedure to check the consistency and the accuracy of these fitting equations for better approximation of the critical temperatures of tethered nanoparticle systems. To do this check, simulations are performed for the 0.62 nm hexa-tethered silica nanoparticle system. First, the system is initialized with a single gas phase system at a temperature $T > T_c + 150$ K (The calculated value of the T_c is obtained from the fitting equations). Then during the course of the simulation, the temperature of the system is cooled gradually until $T > T_c + 10$ K and the system is equilibrated. The potential energy profile and the simulation snapshots are then analyzed to explore the coexistence behavior in a more detailed manner. Fig 6.20 (a) shows the simulation snapshot of the single gas phase system which has a temperature of $T > T_c + 150$ K. Figure 6.20 (b), 6.20 (c), and 6.20 (d) shows the simulation snapshots after gradual cooling of the system temperature from the initial state (i.e. $T > T_c + 150$ K). Both from figure 6.20 (b) and 6.20 (c), it can be seen that at $T > T_c + 50$ K and $T > T_c + 40$ K, the system still maintained a single gas phase with no vapor-liquid coexistence. But at $T > T_c + 10$ K, a small degree of vapor-liquid coexistence has occurred in the system which can be seen from fig 6.20 (d).

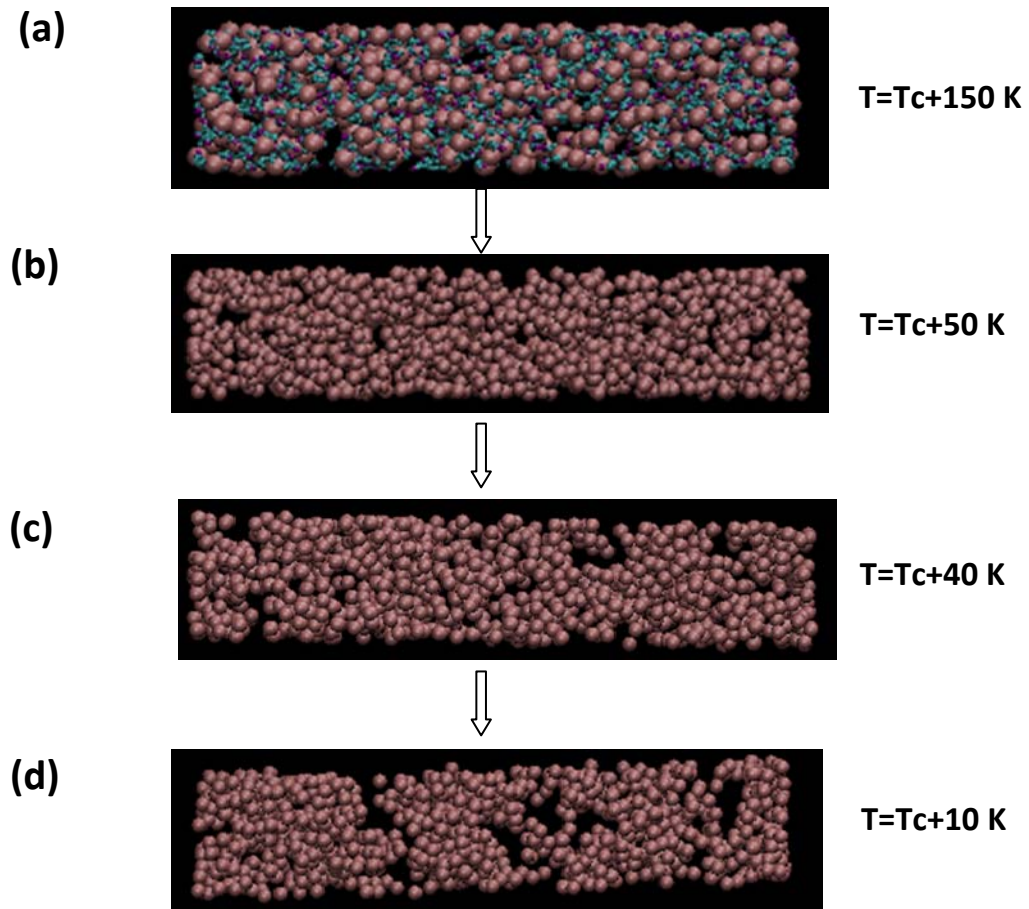


Fig 6.20. Simulation snapshots of hexa-tethered silica nanoparticle system at different temperatures above the estimated critical temperature. (a) $T = T_c + 150 \text{ K}$ (single gas phase), (b) $T = T_c + 50 \text{ K}$ (single gas phase), (c) $T = T_c + 40 \text{ K}$ (single gas phase), (d) $T = T_c + 10 \text{ K}$ (little vapor-liquid coexistence). For (b), (c) and (d) tethers are removed for the ease of visualization

Figure 6.21 shows the plot of the potential energy (PE) of the system as a function of temperature during the gradual cooling procedure. A change in the slope of the curve has been observed at a temperature which is 25 K above the critical temperature ($T > T_c + 25 \text{ K}$) of the system predicted by the fitting equations. We assumed that this temperature i.e. $T > T_c + 25 \text{ K}$ from where the slope of the potential energy curve has been changed is probably the point from where the

phase coexistence started and that temperature might be the actual critical temperature of the hexa-tethered system.

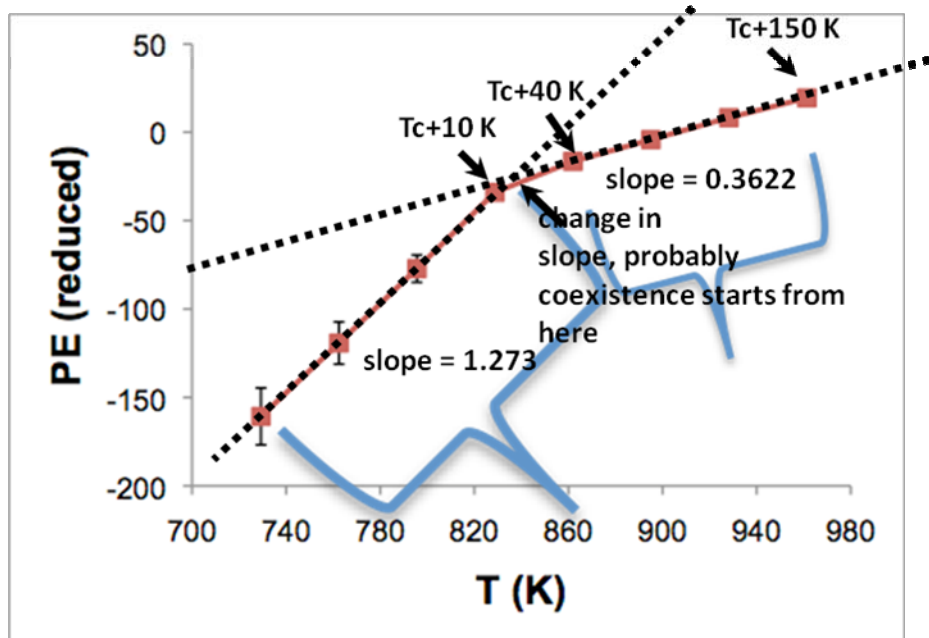


Fig 6.21. Potential energy profile of the hexa-tethered silica nanoparticle system as a function of temperature during the gradual cooling procedure

So, our observation is that the fitting equations might under predict the T_c by ~ 25 K for the hexa-tethered silica nanoparticle system and we think that this under prediction is reasonable as it is only a 4% variation from the calculated critical temperature by the fitting equations. This procedure along with the quench molecular dynamics technique can provide a better approximation of the critical temperature of the tethered nanoparticle systems.

CHAPTER 7

CONCLUSIONS

Volume-quench molecular dynamics approach has been applied to investigate the vapor-liquid coexistence behavior of alkane-tethered generic nanosphere system and alkane-tethered amorphous silica nanoparticle system. We have used coarse-grained model of tethered nanoparticle system which is meant to be generic enough to be applicable over a wide range of systems, yet specific enough such that there is a clear, direct relation to physical systems. The primary purpose of this study is to understand the balance between nanoparticle-polymer interactions and to explore the various trends in vapor-liquid equilibrium behavior of the tethered nanoparticle systems at various anisotropic conditions. We found that the critical temperatures of these systems decrease with the increase in the number of grafted chains on the nanoparticle surface. This observation can be explained by the steric effect the polymers have as the grafting density is increased. We observed that the critical temperature decreases with the increase in tether lengths, which is due to the tethers sterically hindering the structural aggregation of nanoparticles, resulting in the effective screening of strong nanoparticle interactions. This behavior matched with trends obtained from a previously published vapor-liquid equilibrium study of tethered nanoparticle systems [86] and also this observation is inverse of what is typically seen in pure alkane fluids [81]. Also we found that the critical temperature of the system with higher grafting density (for hexa-tethered system with $n_{\text{totalbeads}} = 30$) more closely matches pure dodecane than pure nanoparticle.

We have also investigated the phase behavior of the hexa-tethered silica nanoparticle system as a function of nanoparticle diameter. We found that the critical temperature significantly increases with the increase in nanoparticle diameter. The primary reason behind the increase in critical temperature is due to the significant increase in nanoparticle-nanoparticle interaction combined with the increased nanoparticle surface area. The vapor-liquid equilibrium behavior as a function of planar angle (θ) between tethers is also investigated for di-tethered system. It has been found that with the increase in the planar angle, the critical temperature of the tethered nanoparticle system decreases because of the effective screening of the nanoparticle interactions associated with the increasing angle. Overall, from our calculations of the vapor-liquid phase coexistence of the alkane tethered nanoparticle systems some very interesting trends can be predicted, which may be very useful for the future utilization of these nano-building blocks in processing applications. Also from this work it is found that attaching polymer grafts to the nanoparticle can alter the properties of the resulting system, which can be significantly different than each individual system.

BIBLIOGRAPHY

- [1] Busbee BD, Obare SO, Murphy CJ. An improved synthesis of high-aspect-ratio gold nanorods. *Adv Mater.* 2003;15:414-+.
- [2] Jana NR, Gearheart L, Murphy CJ. Wet chemical synthesis of silver nanorods and nanowires of controllable aspect ratio. *Chem Commun.* 2001:617-8.
- [3] Hess HF, Pettibone D, Adler D, Bertsche K, Nordquist KJ, Mancini DP, et al. Inspection of templates for imprint lithography. *J Vac Sci Technol B.* 2004;22:3300-5.
- [4] Glotzer SC. Some assembly required. *Science.* 2004;306:419-20.
- [5] Glotzer SC. Self-assembly of patchy particles and colloidal "molecules": Insights from in silico. *Abstr Pap Am Chem S.* 2005;229:U742-U.
- [6] Glotzer SC, Solomon MJ. Anisotropy of building blocks and their assembly into complex structures. *Nat Mater.* 2007;6:557-62.
- [7] Kamien RD. Topology from the bottom up. *Science.* 2003;299:1671-3.\
- [8] Song T, Dai S, Tam KC, Lee SY, Goh SH. Aggregation behavior of C-60-end-capped poly(ethylene oxide)s. *Langmuir.* 2003;19:4798-803.
- [9] Glotzer SC, Anderson JA. Nanoparticle Assembly Made to Order. *Nat Mater.* 2010;9:885-7.
- [10] Akcora P, Liu H, Kumar SK, Moll J, Li Y, Benicewicz BC, et al. Anisotropic self-assembly of spherical polymer-grafted nanoparticles. *Nat Mater.* 2009;8:354-U121.
- [11] Glotzer SC, Horsch MA, Iacovella CR, Zhang ZL, Chan ER, Zhang X. Self-assembly of anisotropic tethered nanoparticle shape amphiphiles. *Curr Opin Colloid In.* 2005;10:287-95.
- [12] Iacovella CR, Horsch MA, Zhang Z, Glotzer SC. Phase diagrams of self-assembled mono-tethered nanospheres from molecular simulation and comparison to surfactants. *Langmuir.* 2005;21:9488-94.
- [13] Bockstaller MR, Mickiewicz RA, Thomas EL. Block copolymer nanocomposites: Perspectives for tailored functional materials. *Adv Mater.* 2005;17:1331-49.

- [14] Chan ER, Ho LC, Glotzer SC. Computer simulations of block copolymer tethered nanoparticle self-assembly. *J Chem Phys.* 2006;125.
- [15] Jayaraman A, Schweizer KS. Effective Interactions and Self-Assembly of Hybrid Polymer Grafted Nanoparticles in a Homopolymer Matrix. *Macromolecules.* 2009;42:8423-34.
- [16] Jayaraman A, Schweizer KS. Structure and assembly of dense solutions and melts of single tethered nanoparticles. *J Chem Phys.* 2008;128.
- [17] Jayaraman A, Schweizer KS. Effect of the number and placement of polymer tethers on the structure of concentrated solutions and melts of hybrid nanoparticles. *Langmuir.* 2008;24:11119-30.
- [18] Vangunsteren WF, Berendsen HJC. Computer-simulation of molecular-dynamics - methodology, applications, and perspectives in chemistry. *Angewandte Chemie-International Edition in English.* 1990;29:992-1023.
- [19] Allen MP, Tildesley DJ. *Computer simulation of liquids*: Clarendon Press; 1989.
- [20] Hansson T, Oostenbrink C, van Gunsteren WF. Molecular dynamics simulations. *Curr Opin Struc Biol.* 2002;12:190-6.
- [21] Cuendet MA, van Gunsteren WF. On the calculation of velocity-dependent properties in molecular dynamics simulations using the leapfrog integration algorithm. *J Chem Phys.* 2007;127.
- [22] Zhang ZL, Horsch MA, Lamm MH, Glotzer SC. Tethered nano building blocks: Toward a conceptual framework for nanoparticle self-assembly. *Nano Lett.* 2003;3:13416.
- [23] Gelb LD, Muller EA. Location of phase equilibria by temperature-quench molecular dynamics simulations. *Fluid Phase Equilibr.* 2002;203:1-14.
- [24] Avila CL, Drechsel NJD, Alcantara R, Villa-Freixa J. Multiscale Molecular Dynamics of Protein Aggregation. *Current Protein & Peptide Science.* 2011;12:221-34.
- [25] Carmichael SP, Shell MS. A New Multiscale Algorithm and Its Application to Coarse-Grained Peptide Models for Self-Assembly. *J Phys Chem B.* 2012;116:8383-93.

- [26] Chang K-S, Chung Y-C, Yang T-H, Lue SJ, Tung K-L, Lin Y-F. Free volume and alcohol transport properties of PDMS membranes: Insights of nano-structure and interfacial affinity from molecular modeling. *Journal of Membrane Science*. 2012;417:119-30.
- [27] Li K, Shui ZH, Dai W. Molecular dynamic simulation of structural and mechanical properties of cement hydrates: from natural minerals to amorphous phases. *Materials Research Innovations*. 2012;16:338-44.
- [28] Zheng F, Zhan C-G. Computational Modeling of Solvent Effects on Protein-Ligand Interactions Using Fully Polarizable Continuum Model and Rational Drug Design. *Communications in Computational Physics*. 2013;13:31-60.
- [29] Chu G-W, Gao X, Luo Y, Zou H-K, Shao L, Chen J-F. Distillation studies in a two- stage counter-current rotating packed bed. *Separation and Purification Technology*. 2013;102:62- 66.
- [30] Attarakih M, Abu-Khader M, Bart H-J. Dynamic analysis and control of sieve tray gas absorption column using MATLAB and SIMULINK. *Applied Soft Computing*. 2013;13:1152-69.
- [31] Guo H, Zhang Z, Qian J, Liu Y. Optimization of the liquid-liquid extraction of phosphatidyl-choline from rapeseed oil gums by response surface methodology. *Industrial Crops and Products*. 2013;42:500-6.
- [32] Chen L, Zhu R-J, Fang Y, Yuan P-F, Cao L-Q, Tian Y-L. Vapor-Liquid Equilibrium Data for Carbon Dioxide plus Dimethyl Carbonate Binary System. *Acta Phys- Chim Sin*. 2013;29:11-6.
- [33] Hagen MHJ, Meijer EJ, Mooij GCAM, Frenkel D, Lekkerkerker HNW. Does C-60 Have a Liquid-Phase. *Nature*. 1993;365:425-6.
- [34] Holcomb CD, Clancy P, Thompson SM, Zollweg JA. A critical-study of simulations of the lennard-jones liquid-vapor interface (Vol 75, Pg 185, 1992). *Fluid Phase Equilibr*. 1993;88:303-.
- [35] Smit B, Karaborni S, Siepmann JI. Computer simulations of vapor-liquid phase equilibria of n-alkanes (vol 102, pg 2126, 1995). *J Chem Phys*. 1998;109:352-.
- [36] in' t Veld PJ, Horsch MA, Lechman JB, Grest GS. Liquid-vapor coexistence for nanoparticles of various size. *J Chem Phys*. 2008;129.
- [37] Faradonbeh MR, Abedi J, Harding TG. Comparative study of eight cubic equations of state for predicting thermodynamic properties of alkanes. *J Chem Eng*. 2013;91:101-10.

- [38] Metropolis N, Rosenbluth A, Rosenbluth M, Teller A, Teller E. Equation of state calculations by fast computing machines. *J Chem Phys.* 1953;21.
- [39] Karolczak M. Universal functional-group activity-coefficient model in electrosorption .3. thermodynamical excess mixing functions of the 1-propanol water-system adsorbed at the hg electrode. *Langmuir.* 1990;6:1045-50.
- [40] Karolczak M. Universal functional-group activity-coefficient model in electrosorption .2. electrosorption of 1-propanol at the mercury solution interface. *Langmuir.* 1990;6:863-9.
- [41] Karolczak M. Universal functional-group activity-coefficient model in electrosorption .1. theory. *J Colloid Interf Sci.* 1990;135:97-106.
- [42] Abudour AM, Mohammad SA, Robinson RL, Jr., Gasem KAM. Volume-translated Peng- Robinson equation of state for saturated and single-phase liquid densities. *Fluid Phase Equilib.* 2012;335:74-87.
- [43] Esquiroz-Molina A, Georgaki S, Stuetz R, Jefferson B, McAdam EJ. Influence of pH on gas phase controlled mass transfer in a membrane contactor for hydrogen sulphide absorption. *Journal of Membrane Science.* 2013;427:276-82.
- [44] Dumitrache DC, De Schutter B, Huesman A, Dulf E. Modeling, analysis, and simulation of a cryogenic distillation process for C-13 isotope separation. *Journal of Process Control.* 2012;22:798-808.
- [45] Boal AK, Ilhan F, DeRouchey JE, Thurn-Albrecht T, Russell TP, Rotello VM. Self-assembly of nanoparticles into structured spherical and network aggregates. *Nature.* 2000;404:746-8.
- [46] Glotzer SC, Solomon MJ, Kotov NA. Self-assembly: From nanoscale to microscale colloids. *Aiche J.* 2004;50:2978-85.
- [47] Iacovella CR, Horsch MA, Glotzer SC. Local ordering of polymer-tethered nanospheres and nanorods and the stabilization of the double gyroid phase. *J Chem Phys.* 2008;129.
- [48] Keys AS, Iacovella CR, Glotzer SC. Characterizing Structure Through Shape Matching and Applications to Self-Assembly. *Annu Rev Condens Ma P.* 2011;2:263-85.

- [49] Larson RG. Molecular Simulation of Ordered Amphiphilic Phases. *Chem Eng Sci.* 1994;49:2833-50.
- [50] Nguyen TD, Zhang ZL, Glotzer SC. Molecular simulation study of self-assembly of tethered V-shaped nanoparticles. *J Chem Phys.* 2008;129.
- [51] Horsch MA, Zhang ZL, Glotzer SC. Self-assembly of polymer-tethered nanorods. *Phys Rev Lett.* 2005;95.
- [52] Horsch MA, Zhang ZL, Glotzer SC. Simulation studies of self-assembly of end- tethered nanorods in solution and role of rod aspect ratio and tether length. *J Chem Phys.* 2006;125.
- [53] Iacovella CR, Keys AS, Glotzer SC. Self-assembly of soft-matter quasicrystals and their approximants. *P Natl Acad Sci USA.* 2011;108:20935-40.
- [54] Kumar SK, Krishnamoorti R. Nanocomposites: Structure, Phase Behavior, and Properties. *Annu Rev Chem Biomol.* 2010;1:37-58.
- [55] Iacovella CR, Glotzer SC. Phase behavior of ditethered nanospheres. *Soft Matter.* 2009;5:4492-8.
- [56] Zhang ZL, Keys AS, Chen T, Glotzer SC. Self-assembly of patchy particles into diamond structures through molecular mimicry. *Langmuir.* 2005;21:11547-51.
- [57] Valisko M, Varga T, Baczoni A, Boda D. The structure of strongly dipolar hard sphere fluids with extended dipoles by Monte Carlo simulations. *Mol Phys.* 2010;108:87-96.
- [58] Bartke J, Hentschke R. Phase behavior of the Stockmayer fluid via molecular dynamics simulation. *Phys Rev E.* 2007;75.
- [59] Phillips CL, Iacovella CR, Glotzer SC. Stability of the double gyroid phase to nanoparticle polydispersity in polymer-tethered nanosphere systems. *Soft Matter.* 2010;6:1693-703.
- [60] Srivastava S, Agarwal P, Archer LA. Tethered Nanoparticle-Polymer Composites: Phase Stability and Curvature. *Langmuir.* 2012;28:6276-81.
- [61] Jiao Y, Akcora P. Assembly of Polymer-Grafted Magnetic Nanoparticles in Polymer Melts. *Macromolecules.* 2012;45:3463-70.
- [62] Kai W, Hua L, Dong T, Pan P, Zhu B, Inoue Y. Polyhedral oligomeric silsesquioxane- and fullerene-end-capped Poly(epsilon-caprolactone). *Macromol Chem Phys.* 2008;209:1191-7.

- [63] Song T, Goh SH, Lee SY. Mechanical behavior of double-C60-end-capped poly(ethylene oxide). *Polymer*. 2003;44:2563-7.
- [64] Westenhoff S, Kotov NA. Quantum dot on a rope. *J Am Chem Soc*. 2002;124:2448-9.
- [65] Huang JC, He CB, Xiao Y, Mya KY, Dai J, Siow YP. Polyimide/POSS nanocomposites: interfacial interaction, thermal properties and mechanical properties. *Polymer*. 2003;44:4491-9.
- [66] Lu X, Lu N, Gao J, Jin X, Lu C. Synthesis and properties of ZnS/polyimide nanocomposite films. *Polymer International*. 2007;56:601-5.
- [67] Wang K, Chen L, Wu JS, Toh ML, He CB, Yee AF. Epoxy nanocomposites with highly exfoliated clay: Mechanical properties and fracture mechanisms. *Macromolecules*. 2005;38:788-800.
- [68] Lee GW, Park M, Kim J, Lee JI, Yoon HG. Enhanced thermal conductivity of polymer composites filled with hybrid filler. *Composites Part a-Applied Science and Manufacturing*. 2006;37:727-34.
- [69] Zhang C, Li Q, Ye Y. Preparation and characterization of polypyrrole/nano-SrFe₁₂O₁₉ composites by in situ polymerization method. *Synthetic Metals*. 2009;159:1008-13.
- [70] Iacovella CR, Keys AS, Horsch MA, Glotzer SC. Icosahedral packing of polymer- tethered nanospheres and stabilization of the gyroid phase. *Phys Rev E*. 2007;75.
- [71] Knischka R, Dietsche F, Hanselmann R, Frey H, Mulhaupt R, Lutz PJ. Silsesquioxane-based amphiphiles. *Langmuir*. 1999;15:4752-6.
- [72] Talapin DV, Shevchenko EV, Bodnarchuk MI, Ye XC, Chen J, Murray CB. Quasicrystalline order in self-assembled binary nanoparticle superlattices. *Nature*. 2009;461:964-7.
- [73] Li TING, Sknepnek R, Macfarlane RJ, Mirkin CA, de la Cruz MO. Modeling the Crystallization of Spherical Nucleic Acid Nanoparticle Conjugates with Molecular Dynamics Simulations. *Nano Lett*. 2012;12:2509-14.
- [74] Wood WW, Parker FR. Monte carlo equation of state of molecules interacting with the lennard- jones potential. i. supercritical isotherm at about twice the critical temperature. *Journal Name: Journal of Chemical Physics (US); Journal Volume: Vol: 27; Other Information: Orig Receipt Date: 31-DEC- 58. 1957:Medium: X; Size: Pages: 720-33.*

- [75] Alder BJ, Wainwright TE. Phase Transition for a Hard Sphere System. *The Journal of Chemical Physics*. 1957;27:1208-9.
- [76] Bolhuis PG, Louis AA, Hansen JP, Meijer EJ. Accurate effective pair potentials for polymer solutions. *J Chem Phys*. 2001;114:4296-311.
- [77] Likos CN. Effective interactions in soft condensed matter physics. *Physics Reports-Review Section of Physics Letters*. 2001;348:267-439.
- [78] Jabbarzadeh A, Atkinson JD, Tanner RI. Effect of molecular shape on rheological properties in molecular dynamics simulation of star, H, comb, and linear polymer melts. *Macromolecules*. 2003;36:5020-31.
- [79] Bird RB, Armstrong RC, Hassager O. *Dynamics of polymeric liquids*. Vol. 1, 2nd Ed. : Fluid mechanics 1987.
- [80] Girifalco LA. Molecular-Properties of C-60 in the Gas and Solid-Phases. *J Phys Chem-Us*. 1992;96:858-61.
- [81] Martin MG, Siepmann JI. Transferable potentials for phase equilibria. 1. United-atom description of n-alkanes. *J Phys Chem B*. 1998;102:2569-77.
- [82] Chan ER, Zhang X, Lee CY, Neurock M, Glotzer SC. Simulations of tetra-tethered organic/inorganic nanocube-polymer assemblies. *Macromolecules*. 2005;38:6168-80.
- [83] Lee CK, Hua CC. Nanoparticle interaction potentials constructed by multiscale computation. *J Chem Phys*. 2010;132.
- [84] Anderson JA, Lorenz CD, Travesset A. General purpose molecular dynamics simulations fully implemented on graphics processing units. *J Comput Phys*. 2008;227:5342-59.
- [85] Paricaud P, Predota M, Chialvo AA, Cummings PT. From dimer to condensed phases at extreme conditions: Accurate predictions of the properties of water by a Gaussian charge polarizable model. *J Chem Phys*. 2005;122.
- [86] Peng Y, McCabe C. Molecular simulation and theoretical modeling of polyhedral oligomeric silsesquioxanes. *Mol Phys*. 2007;105:261-72.

- [87] Sun LX, Zhao HG, Kiselev SB, McCabe C. Predicting mixture phase equilibria and critical behavior using the SAFT-VRX approach. *J Phys Chem B*. 2005;109:9047-58.
- [88] Orbey H, Sandler SI. *Modeling Vapor-Liquid Equilibria*. Cambridge University Press, 1998.